Effect of γ-Irradiation on Ruthenium-Morin Nanocomposite for Trace Detection of Ce(IV), Ce(III) and Dy(III)

Pritam Singh[1], Zarina Ansari[1], Santanu Ray[2], Bilwadal Bandyopadhyay[3], and Kamalika Sen[1*]

[1]Department of Chemistry, University of Calcutta, 92, A. P. C. Road, Kolkata 700009, India
[2]Surface Analysis Laboratory, School of Environment and Technology, University of Brighton, Brighton, BN2 4GJ, United Kingdom
[3]CMP Division, Saha Institute of Nuclear Physics, 1/AF Bidhannagar, Kolkata 700064, India
*E-mail: kamalchem.roy@gmail.com

ABSTRACT

The article reports on the generation of Ru-morin nanocomposites using a simple methodology in presence and in absence of γ-irradiation. The nanocomposites were characterized using several techniques including, N_2 adsorption-desorption, Brunauer−Emmett−Teller (BET) method, transmission electron microscopy (TEM), Fourier transform infra-red (FTIR) spectroscopy, powder X-ray diffractometric (XRD) technique, dynamic light scattering (DLS) and X-ray photoelectron spectroscopic (XPS) methods. The results revealed the production of comparatively smaller sized particles with smaller pores when prepared in presence of energetic γ-irradiation. The irradiated nanocomposite was found to be an eligible candidate for analytical sensing of Ce(IV), Ce(III) and Dy(III) out of a set of different lanthanoids. The lowest values of limit of detection (LOD) out of all the pH conditions for Ce(IV), Ce(III) and Dy(III) were 0.09 μM (at pH 12), 0.08 μM (at pH 12) and 5.37 μM (at pH 2) respectively using absorption spectroscopy. The LOD of Ce(IV) at pH 7 was found to be 0.35 μM by fluorescence spectroscopic method. It is established that the sensing is a pH dependent phenomenon which enables a selective and mutually exclusive sensing of these three lanthanoids individually. The study was also extended towards two environmental samples viz., tap water and ground water with significant recovery of Ce(IV), Ce(III) and Dy(III) from tap water and Ce(IV) and Dy(III) from ground water.

Keywords: Ruthenium; morin; gamma irradiation; trace concentration; lanthanoids; absorbance;

1. Introduction

Nanoparticles are known to carry different unique features as compared to their bulk analogues. The attainability of variable sizes, shapes and high surface to volume ratio make them applicable in different branches of science. Growing interest towards synthesis of nanoparticles are being observed due to their promising applications in different fields like, catalysis, sensing, nano-electronics and most importantly in bio-medical field [1-6]. The need to develop cleaner methodologies for generating nanoparticles was therefore perceived and as a result, a vastly developing field of green nanotechnology is emerging currently. In this direction, bio-synthesis of nanoparticles has drawn attention of the scientists due to its cost-effective, environment friendly and efficient production route. For the synthesis of nanocomposite materials, the main concern lies on few important parameters like, chemical composition, shape, size and mono-dispersity of the nano-materials [2].

Ruthenium is a transition element of noble metal group that has been widely used in catalysis, fuel cells, electro-catalysis [3], hydrogen storage [4] and anti-bacterial activity [5]. There are some reports on the sensing of few gases, like H_2, O_2, C_2H_5OH, H_2S, NH_3, acetone, NO_2, etc., based on Ru-nanocomposites as well [6-11]. A variety of conventional methods are available for the preparation of Ru-based nanocomposites [1] which contradict the mandate of green synthesis. Additionally, control over the shape and size of the nanomaterials using those methods are controversial. Due to the current scenario associated with our environmental issues, scientists are mainly focusing on the green synthesis of such metal-nanoparticles. Xiaojuan et al. reported a one-step microwave assisted synthesis of Ru-nanoparticle wherein dodecacarbonyltriruthenium and carbon nano tube (CNT) were mixed together and then fluidized with argon for 2 h at room temperature, and then the mixture was placed in a domestic microwave oven operating at 2.45 GHz with a power of 800 W [12]. In another report, Dikhtiarenko et al. used hydrothermal technique (~ 180 °C) using $RuCl_3$ as precursor with trisodium citrate and ascorbic acid as both reducing and capping agents. The reaction was performed at pH 6 with 24 h reaction time [1]. Kannan and Sundrarajan prepared RuO_2 nanoparticles using $RuCl_3$ as precursor and *A. indica* leaf extracts as a precipitant upon stirring for 2 h at 80 °C. The solid material was centrifuged at 10,000 rpm, washed and finally obtained after calcination at 600 °C [2]. Zhao et al. reported the synthesis of Ru/graphene composite taking $RuCl_3$ as a source of ruthenium and graphene oxide

(GO) as a starting material without using any organic solvent. The mixture was stirred for 1 h and heated at 400 °C for 2 h under an autoclave [13].

One of the greener route to the synthesis of metal-nanoparticles is using gamma irradiation technique as it produces a huge number of free radicals in the solution that accelerate the reduction of metal ion to its nano state [14]. At the same time the particle size and crystal structure can also be adjusted depending on the time and strength of the radiation source employed [15,16]. Due to incorporation of gamma radiation into water, radiolysis takes place forming hydrated electrons (e^-_{aq}), $H^{\cdot}$ and $OH^{\cdot}$ radicals [17]. Herein hydrated electrons are mainly responsible for the uniform reduction of metal from its ionic form to its zero-valent nanostate [15-18].

In recent green synthesis approach, flavonoids are considered as a good reducing and stabilizing candidates in generating metal-nanoparticle assemblies. Different applications in clinical and biological fields have also grown continued interests of flavonoids [19]. Morin, one of many such flavonoid, is a yellow colored polyphenol obtained from natural sources like, *Maclurapomifer*a, *Macluratinctoria* and from leaves of *Psidium guajava* [20].

Selective identification of individual lanthanoids from mixed sources is a difficult task, due to lanthanoid contractions with increasing atomic numbers forcing atomic sizes of these elements not to vary substantially. For nearly a century, Ion Selective Electrodes (ISE) have been an important tool for the selective detection of lanthanoids. The ever growing interest about this instrumentation is due to its low cost, reliable methodology and low limit of detection for the sensing of the analyte. However, shortcomings like, significant interferences and a very narrow range of working pH, makes this method unfavorable [21] in many cases. Some sophisticated instruments can also be used to detect ultra trace amount of lanthanoids. Some of the reported methods for estimation of lanthanoids are tabulated in Table 1 along with the limit of detection (LOD) values.

In the present work we have synthesized ruthenium-morin nanocomposites at room temperature, taking $RuCl_3$ as a source of ruthenium and morin as a stabilizing agent. The synthesis was carried out both in presence and in absence of gamma irradiation. The nanomaterials so obtained were then characterized using N_2 adsorption-desorption and BET analysis, TEM, FTIR, XPS, etc., techniques. The irradiated nanocomposite solution was found suitable to selectively

determine trace amounts of Ce(IV), Ce(III) and Dy(III) from a set of different lanthanoids in different pH medium without addition of any foreign substances. The sensing was completely pH dependent and it is possible to have isolate conditions for detection and estimation of the individual metal ions by varying the pH of the medium. The sensing was also found suitable with a significant recovery of Ce(IV), Ce(III) and Dy(III) from tap water and Ce(IV) and Dy(III) from ground water.

2. Experimental Section

2.1. Materials

Ruthenium(III) chloride hydrate ($RuCl_3 \cdot xH_2O$) (38.0 – 42.0 % Ru) and morin hydrate (2-(2,4-dihydroxyphenyl)-3,5,7-trihydroxychromen-4-one) (≥ 85.0 %) were obtained from Sigma Aldrich, USA. Ammonium cerium(IV) sulfate dihydrate ($Ce(NH_4)_4(SO_4)_4 \cdot 2H_2O$) (≥ 94.0 %), cerium trichloride ($CeCl_3$) (≥ 99.99 %), dysprosium(III) nitrate hydrate ($Dy(NO_3)_3 \cdot xH_2O$) (99.9 %), samarium(III) nitrate hexahydrate ($Sm(NO_3)_3 \cdot 6H_2O$) (99.9 %), lanthanum(III) chloride hydrate ($LaCl_3 \cdot xH_2O$) (99.9 %) and gadolinium(III) chloride ($GdCl_3$) (99.0 %) were obtained from Sigma Aldrich, USA. Folin & Ciocalteu's phenol reagent and gallic acid monohydrate ($(HO)_3C_6H_2CO_2H \cdot H_2O$) (98.0 %) were obtained from HiMedia Laboratories Pvt. Ltd., India. 1, 10 phenanthroline monohydrate (≥ 99.5 %) and hydroxylammonium chloride (≥ 99.0 %) were obtained from Sigma Aldrich, USA. L-tryptophan ($C_{11}H_{12}N_2O_2$) (99.0 %) was obtained from Sisco Research Laboratories Pvt. Ltd., India. Sodium carbonate anhydrous (Na_2CO_3) (≥ 99.5 %) was obtained from Merck Specialities Pvt. Ltd., India. Sodium hydroxide (NaOH) (≥ 97.0 %) was obtained from Merck Life Science Private Limited, India. Spectroscopic grade ethanol (99.9 %) was obtained from Spectrochem Pvt. Ltd. India. To study the interferences from other ions, we chose iron(III) nitrate nonahydrate ($Fe(NO_3)_3.9H_2O$) (≥ 98.0 %), cobalt(II) chloride ($CoCl_2$) (≥ 98.0 %), nickel(II) sulfate hexahydrate ($NiSO_4.6H_2O$) (99.99%), copper sulfate pentahydrate ($CuSO_4$.5H2O) (≥98%), zinc sulfate heptahydrate ($ZnSO_4.7H_2O$) (99.5%) which were purchased from Merck Specialities Pvt. Ltd., India. We also chose samarium(III) nitrate hexahydrate ($Sm(NO_3)_3 \cdot 6H_2O$) (99.9 %), lanthanum(III) chloride hydrate ($LaCl_3 \cdot xH_2O$) (99.9 %), gadolinium(III) chloride ($GdCl_3$) (99.0 %) which were obtained from Sigma Aldrich, USA. To see the applicability of the present technique of sensing of lanthanoids, we have taken tap water

and ground water from the area of Rajabazar, Kolkata, India. All other reagents were of AR grade and used as obtained.

2.2. Apparatus

Absorption data was obtained using Perkin-Elmer lambda 25 UV-Vis spectrophotometer. A luminescence spectrometer LS-55B (Perkin-Elmer, USA) was used for monitoring fluorescence property. Nitrogen adsorption-desorption isotherms were measured at a liquid nitrogen temperature (77 K) using a Quantachrome surface area analyzer. The specific surface areas and pore diameters were calculated by the Brunauer−Emmett−Teller (BET) method. TEM images were obtained by a JEOL JEM 2100 HR with EELS transmission electron microscopy. The Fourier transform infra-red (FTIR) spectra of the samples were recorded from 400 to 4000 cm^{-1} on a Perkin Elmer FT-IR 783 spectrophotometer having resolution 1 cm^{-1} using KBr pellets. A Mettler Toledo digital balance correct up to fourth decimal place was used for measuring the weights. A centrifuge machine Remi Elektrotechnik Ltd. R-4C was used to separate the supernatant solution of the nanoparticle. X-ray diffraction (XRD) was measured using X-PERT-PRO Panalytical diffractometer to confirm the actual phase of the prepared material. The hydrodynamic radii of the nanocomposite materials were estimated using Malvern, Zetasizer, Nano S, Model- ZEN 1600 dynamic light scattering (DLS) instrument. X-ray photoelectron spectroscopy (XPS) measurement was carried out using a Thermo Scientific ESCALAB 250 Xi system. A digital Mettler Toledo Seven Compact pH/ion meter was used to measure and adjust the pH of the solutions. A radiation chamber (obtained from Board of Radiation and Isotope Technology) with ^{60}Co source of strength 3.7 kCi and cylindrical sample chamber with diameter of 10.6 cm and height 14.2 cm were used for gamma irradiation.

2.3. Synthesis of ruthenium-morin nanocomposite without γ-irradiation (Set A)

The ruthenium-morin nanocomposite was synthesized in a simple one step process by mixing solutions of $RuCl_3$ and morin at pH 12. 5 mL of 10 mM $RuCl_3$ solution was prepared in triple distilled water. The temperature of water was kept in the range of 15 to 18 °C, as at high temperature, the solubility of $RuCl_3$ is relatively weak. On the other hand, 5 mL of 10 mM morin solution was prepared in alcohol. Then, $RuCl_3$ solution was added to the morin solution and the

pH of the mixture was finally adjusted to 12 and left undisturbed overnight to complete the reaction. A part of the colloidal solution was then taken for spectral sensing studies. Another part was used for collecting the solid nanoparticles for which, the colloidal solution was allowed to dry. The solid so obtained was washed several times using water-alcohol mixture (1:1) until the supernatant was colorless. Finally, the solid material was dried under IR lamp for their characterization, viz., FTIR, powder XRD, N_2 adsorption-desorption experiment and XPS analysis.

2.4. Synthesis of ruthenium-morin nanocomposite with γ-irradiation (Set B)

To find the effect of gamma irradiation on the morphology of ruthenium-morin nanocomposite, 5 mL of 10 mM $RuCl_3$ solution was added to 5 mL of 10 mM morin solution and then the pH was adjusted to 12 as above. The solution mixture was then kept in a gamma chamber for 24 h having dose rate 1.594 kGy/h. A part of the irradiated solution was taken for spectral sensing studies. The other part was collected, and the solid material was washed and dried as in the previous case.

3. Characterization

3.1. Absorption spectroscopy

Absorption spectroscopy was utilized to get best condition for the formation of ruthenium-morin nanocomposite and used as a tool for the sensing and interference study. The time scan profile obtained using absorption spectroscopy helped to estimate possible mechanism behind the formation of nanocomposite. In addition, it was also used to calculate the amount of unreacted morin and ruthenium(III) in Set A and Set B nanocomposite solutions. The alcoholic solution of morin has its characteristic absorbance at around 330 nm. In order to search the best condition for the nanocomposite formation, solutions of different pH (viz., 5, 7, 9 and 12) were prepared using dilute HCl or dilute NaOH solutions. 0.2 mL of 10 mM morin solution was added to 2.5 mL of the pH adjusted solutions taken in quartz cuvette for spectrophotometric studies. 1 mM $RuCl_3$ solution was gradually added (in 0.01 mL portions) into the morin containing solutions for spectral analysis. Estimation of unreacted morin was carried out by Folin-Ciocalteu method [35] and a distinct peak was obtained at 770 nm. To estimate ruthenium(III), a mixture of 1,10-phenanthroline and hydroxylammonium chloride was used giving a characteristic peak at 448 nm for the formation of *tris*-(1,10-phenanthroline) ruthenium(II) complex.

3.2. Estimation of total unreacted polyphenol

The total amount of unreacted polyphenol in Set A and Set B was estimated using a well known Folin-Ciocalteu method taking gallic acid as standard [35-38]. According to this method, solutions of gallic acid of varying concentrations (0.01-0.2 mM), 2% sodium carbonate (Na_2CO_3) and 50% Folin-Ciocalteu (FC) reagent were prepared. Then with the help of gallic acid solutions a calibration curve was obtained in presence of Na_2CO_3 and FC reagent. For measuring the unreacted polyphenol, the supernatant and the combined washings were pooled together and an aliquot (0.5 mL) of this solution of Set A and Set B was added to FC reagent (0.5 mL) and 2 % Na_2CO_3 solution (4 mL) mixture. The reaction was then incubated at room temperature (21 ± 1 °C) for an hour. Finally, the absorbance value was recorded at 770 nm. With the help of a previous standard gallic acid calibration plot, the amount of total polyphenol remaining unreacted in the supernatant after nano formation was estimated.

3.3. Estimation of unreacted ruthenium(III)

The total amount of unreacted ruthenium(III) was estimated with the help of 1,10-phenanthroline as a complexing agent and hydroxylammonium chloride as a reducing agent [39]. Initially, a calibration curve was drawn by taking known amounts of ruthenium(III) solution into the mixture of excess amount of the above two reagents. Then a known amount of supernatant and the combined washing solution of Set A and Set B (as before) were added to the same reagent mixture. Then all the reaction mixtures were allowed to heat at ~100 °C for 10 to 15 min. Finally, the absorbance of the solution was measured at 448 nm. The amount of unreacted ruthenium(III) was estimated using a suitable calibration plot.

3.4. Band gap and Tauc plot

With the help of absorption spectra, we were able to construct Tauc plots for determination of the band gap of the ruthenium-morin nanocomposites at different pH using the following relation of energy of incident photon (hν) and absorption coefficient (α):

$$(\alpha h\nu)^{\frac{1}{m}} = C(h\nu - E_g) \quad \text{.....(1)}$$

Where, C = constant;

E_g= band gap of the nanomaterial;

m = depends on the type of transition; 1/2 for direct allowed transition; 3/2 for direct forbidden transition; 2 for indirect allowed transition and 3 for indirect forbidden transition.

If we plot $(\alpha h\nu)^2$ (taking m = 1/2) vs. hν, we could get a linear segment. By extrapolating the line to α = 0 value, it provides an intercept on the hν axis which gives the band gap (E_g) of the nanoparticle. Tauc plot was also obtained to measure the change in the band gap in the nanomaterials after performing the sensing experiment. As band gap varies inversely with the particle size due to confinement of electrons in a nano-scale (quantum size effect) [40], a comparative idea of the particle size could also be obtained from this value.

3.5. Fluorescence spectroscopy

Fluorescence spectroscopy helped to determine and confirm the best condition associated with the formation of ruthenium-morin nanocomposites. This spectroscopy was also employed to study the sensing of Ce(IV) at pH 7. Similar to the absorption spectral studies, 0.03 mL of 10 mM morin solution was added to 2.5 mL of pH adjusted solutions and the emission spectra were taken at λ_{em} = 478 nm after excitation at λ_{ex} = 330 nm. Aliquots of 1 mM $RuCl_3$ solution were gradually added to it to study the interaction between morin and $RuCl_3$. For sensing of Ce(IV), the λ_{ex} was kept at 290 nm (considering the absorption spectrum of the nanoparticle solution) and λ_{em} was observed at ~391 nm.

3.6. Quantum yield (φ) calculation

In order to analyze the fluorimetric sensing of Ce(IV) at pH 7 using our nanocomposite, we compared the quantum yield for Ce(IV) at this pH of nanocomposite solution and a blank pH 7 solution. The quantum yield was determined using tryptophan (φ = 0.14) (λ_{ex} = 280 nm) as a standard.

3.7. N_2 adsorption-desorption and BET analysis

This analysis was carried out to determine the specific surface area, pore volume and pore size distribution of the nanoparticles. Firstly, the solid sample was degassed at 300 °C for 3 h at the surface area analyzer instrument. Then the specific surface area of the nanomaterial was obtained with the help of BET method.

3.8. TEM analysis

2 mg of the solid sample was dispersed in 2 mL of mixed solvent (water:alcohol = 1:1) and the mixture was sonicated for 1 h. A drop of this solution was drop-casted on a carbon coated Cu grid. Finally, the grid was dried under IR lamp and then the TEM microscopic images were obtained.

3.9. FTIR analysis

A small amount of the solid sample was mixed thoroughly with dried KBr to make a pellet using a hydraulic press (~5 ton pressure). Then the pellet was placed in the analyzer to get clear idea about the bond vibrations of the material. Metal salt solution treated nanoparticles were also taken and dried for FTIR spectral analysis and confirmation of chemical interactions occurring therein.

3.10. Powder XRD

The powdered nanoparticle samples were taken in a rectangular metal holder and lightly pressed for the X-ray diffraction studies.

3.11. DLS

The sample preparation for DLS is quite similar to that of TEM experiment. Here also 2 mg of the solid sample was dispersed in 2 mL of mixed solvent (water:alcohol = 1:1) and then the mixture was sonicated for 1 h. This solution was diluted ~ 10 times and the DLS measurement was done.

3.12. XPS

Elemental composition and the respective oxidation states of the nanocomposite materials were investigated using XPS analysis. The XPS instrument is equipped with a monochromated Al Kα X-ray source with x-ray spot size 900x900 μm^2. Uniform charge neutralization was provided by multi-mode electrostatic flood source. Full survey scans (step size 1 eV, pass energy 150 eV, dwell time 50 ms and 5 scans) and narrow scans (step size 0.1 eV, pass energy 20 eV, dwell time 100 ms and 15 scans) of Ru3d (binding energy, BE ~280 eV), C1s (BE ~285 eV), N1s (BE ~400 eV) and O1s (BE ~531 eV) were acquired from three separate regions from each sample.

As binding energy of Ru3d merges with BE of C1s, Ru3p (BE ~475 eV) narrow scan was also acquired. Data were analysed using Thermo Avantage Software (Version 5.952) using a smart background.

3.13. Sensing experiment

For the sensing study, three different pH solutions (viz. pH 2, pH 7 and pH 12) were prepared. The nanocomposite solution was taken in these pH adjusted solutions and then the salt solutions of metal ions, La(III), Ce(IV), Ce(III), Sm(III), Gd(III) and Dy(III)) were gradually added into the nanocomposite solution separately. In order to study the sensing ability of the ruthenium-morin nanocomposite (both Set A and Set B), 1 (mM) of each of La(III), Ce(IV), Ce(III), Sm(III), Gd(III) and Dy(III) solutions were prepared in water taking their respective salts by proper weighing.

3.14. Interference study

The interference study was done using both absorption and emission spectroscopy. In order to search the interference from lanthanoids and transition elements, 2 mL of pH adjusted (pH 2, 7 and 12) solutions were taken and treated with requisite amount of the freshly prepared Set B nanocomposite solution. Each interfering metal solution was added to the resulting mixture and treated with the analyte (Ce(IV), Ce(III) or Dy(III)) at equimolar concentrations. Then the resulting experimental solutions were measured under UV-Vis and fluorescence spectroscopy.

3.15. Analyses of environmental samples

Analyses of environmental samples were done in order to check the applicability of the nanocomposite (set B) for environmental samples. We have taken tap water and ground water as environmental samples. pH of the samples were first adjusted to 2, 7 and 12. Then 2 mL of each of the water sample was treated with requisite amount of freshly prepared Set B nanocomposite solution and finally different amount of Ce(IV), Ce(III) or Dy(III) were added to the mixture. The resulting solutions were then analyzed using UV-Vis spectroscopy and compared with a suitable calibration of each of the analytes. The amounts of recovery of the respective analytes were then calculated.

4. Results and Discussion

4.1. Characterization

4.1.1. Absorption spectroscopy

Absorption spectroscopic study reveals that the best condition for nanocomposite formation can be achieved at pH 12, where a sharp increase of absorbance value is observed at 330 nm (Fig. 1). With the help of Benesi-Hildebrand (B-H) equation (equation 2) we obtained the stoichiometry (1:1) and association constant (K_a = 1,235.82 M^{-1}) of the interaction between morin and Ru at pH 12 (Fig. 1 inset).

$$\frac{1}{A-A_0} = \frac{1}{A_1-A_0} + \frac{1}{(A_1-A_0)K_a[M]} \quad \text{..... (2)}$$

Where, A_0 = the absorbance of morin solution in absence of ruthenium; A_1 = absorbance of morin when it is completely bound with ruthenium; A = absorbance of morin with gradual addition of ruthenium; [M] = concentration of ruthenium; K_a = binding/association constant [41].

The absorption spectral changes of morin solution in pH 5, 7 and 9 media with increasing Ru concentration are pictorially described in supplementary file (Fig. S1 to S3).

4.1.2. Mechanism of formation of nanocomposite

The mechanism for the formation of the nanocomposite was analyzed using absorption spectroscopy. Equal volumes of same concentration of aqueous $RuCl_3$ solution and alcoholic morin solution were mixed at pH 12. The absorbance of the resulting solution was measured at λ_{max} = 330 nm continuously upto 4.5 h (Fig. 2). The plot of absorbance vs. time gives a clear idea about the mechanism of the nanocomposite formation. Initially, an increase in the absorbance is observed suggesting an increase in monomer concentration which thereafter passes through a maximum indicating a burst governed by LaMer mechanism. Subsequently, the absorbance value decreases and then again a steep rise in the absorbance is observed which indicates initiation of rapid auto-catalytic growth as described by Finke-Watzky model [42].

4.1.3. Estimation of unreacted polyphenol and ruthenium(III)

From the Folin-Ciocalteu method the total amount of unreacted polyphenol was found to be 3.81 mM and 1.33 mM equivalent of gallic acid for Set A and Set B respectively. Whereas, the amount of unreacted ruthenium(III) was 3.65 mM and 1.24 mM for Set A and Set B respectively.

Considering the initial known concentrations of both morin and Ru, the actual amount of both the entities present in the nanocomposite were calculated and the results are tabulated in Table 2. From these results, we can say that the probable stoichiometry of the metal:polyphenol complex is 1:0.88 for Set A and 1:0.98 for Set B. Table 2 describes the details of the concentration of reacted ruthenium and morin along with the corresponding stoichiometry for both Set A and Set B. These results are in agreement with the data obtained from B-H plot of metal: polyphenol stoichiometry.

4.1.4. Tauc plot and Band gap

The Tauc plot for the interactions between morin and $RuCl_3$ at four different pHs (viz., pH 5, pH 7, pH 9 and pH 12) are presented in Fig. S1 (inset) to S3 (inset) and Fig. S4. The band gap values were than calculated using the equation 1 and are tabulated in Table 3. The increase in band gap value from pH 5 (5.55 eV) to pH 12 (5.68 eV) clearly indicates the decrease in the particle size [43]. Decrease in the particle size leads to increase in the surface to volume ratio of the nanocomposites and eventually its surface activity gradually increases. We have calculated the band gap values of the nanocomposite after treatment with metal ions (viz., Ce(IV), Ce(III) and Dy(III)) (Fig. S5 to S9). The data showed that, for all the three cases the band gap values decreased than that of pristine nanocomposite material suggesting the increase in the particle size due to the incursion of the metals into the microenvironment of the nanocomposite. A detailed discussion about the sensing is described in the "sensing study" section.

4.1.5. Fluorescence spectroscopy

As the absorption spectral data revealed the best condition for the formation of ruthenium-morin nanocomposite only at pH 12, we studied the fluorescence emissions at this particular pH 12 to obtain further evidences in favor of the interaction between morin and $RuCl_3$. Morin has its characteristic fluorescence emission at λ_{em} = 478 nm upon excitation at λ_{ex} = 330 nm. With increasing additions of $RuCl_3$ solution to the alcoholic solution of morin in pH 12 medium, the emission intensity gradually decreases (Fig. 3). From the Stern-Volmer equation (equation 3) and corresponding plot we can arrive at the Stern-Volmer constant (K_{SV} = 9,475.24 M^{-1}). The plot indicates that the quenching is either static or dynamic in nature (Fig. 3 inset).

$$\frac{I_0}{I} = 1 + K_{SV}[Q] \quad \text{.....(3)}$$

Where, I_0 = fluorescence intensity in absence of quencher; I = fluorescence intensity in presence of analyte; K_{SV} = Stern-Volmer constant or quenching constant; [Q] = concentration of quencher.

4.1.6. N_2 adsorption-desorption and BET analysis

The solid nanocomposite from both Set A and Set B were characterized using N_2 adsorption-desorption technique in order to determine the surface properties of the materials. From the adsorption-desorption study, we found that both the materials have similar surface properties giving Type II isotherm with H3 hysteresis loop (Fig. 4). This convex type of isotherm with higher adsorption at high P/P_0 value is generally observed for multilayer adsorption phenomenon. On the other hand H3 hysteresis loop is basically observed for materials containing mesopores [44, 45]. Although, the overall nature of the curve for Set B is similar to that of Set A, but the curve for Set B is steeper at higher P/P_0 value and there is some disturbance observed at the flat portion at lower P/P_0 values. This may be attributed to the fact that, due to gamma irradiation induced synthesis of the nanocomposite, the surface activity of the material was high. Generation of extensive number of free radicals in the medium resulted in altered gas adsorption properties that results in a noisy appearance of the adsorption-desorption pattern at the low pressure region. Using the BET method, the pore sizes of the materials were obtained which are in the mesoporous diameter range having values of 8.33 nm for Set A and 5.96 nm for Set B.

4.1.7. TEM analysis

The nano-dimensions of the particles were confirmed from TEM analysis. The TEM images of Set A and Set B showed frail lattice fringes (Fig. 5A and 6A). The porous nature can also be seen from the TEM images which is in agreement with the N_2 adsorption-desorption experiment. The selected area electron diffraction (SAED) pattern for both of the materials show some blurred spots which may be for weak crystallinity of the materials (Fig. 5B and 6B). The particle size obtained from histogram of the materials for Set A and Set B were found to be ~20 nm and ~15 nm respectively (Fig. 5C and 6C). The smaller particle size in Set B samples is due to the effect of high energy gamma irradiations that hinders in the particle aggregation in the medium [46, 47].

4.1.8. FTIR analysis

Fig. 7 represents the FTIR spectra of pure morin, and ruthenium-morin nanocomposite (both Set A and Set B). Upon interaction with ruthenium both in absence and in presence of gamma irradiation, there is a huge change in the IR spectral region of 1612 to 831 cm^{-1} from that of pure morin. The peak at 1612 cm^{-1} appears in morin sample due to C=O stretching vibration which gets shifted to ~1619-1627 cm^{-1} on reacting with ruthenium. This shift is attributed to the involvement of C=O towards binding with metal. On the other hand, the two closely spaced peaks at 1515 and 1445 cm^{-1} were observed in morin due to aromatic C=C stretching and in plane C-C-H bending, which disappeared on nanocomposite formation in Set A and decreased in intensity in Set B. The peak at 1376 cm^{-1} due to -OH bending vibration and in plane bending vibration of C-O-H group observed in morin completely disappeared in Set B and was slightly blue shifted in Set A. The peaks of 1294 cm^{-1} and 831 cm^{-1} present in morin due to asymmetric stretching of Ph-O bond and twisting of C-O bond respectively disappeared on nanocomposite formation (both Set A and Set B). The peak at 1163 cm^{-1} owing to aromatic C-H bending in morin disappeared in Set A and was found blue shifted in Set B. All these changes may be a clear indication of interaction between morin and ruthenium and that the interaction is mainly prevailing near the aromatic moiety of the morin molecule. The three new peaks in the region of 2067 cm^{-1} to 1867 cm^{-1} may be attributed to the formation of ruthenium carbonyl bond in the nanocomposite. The results with individual band identification are presented in Table 4.

4.1.9. Powder XRD

The powder X-ray diffraction pattern of the two nanocomposites (Set A and Set B) are represented in Fig. S10. The pattern did not show any major diffractions form any of the Sets. This is in contrary to the TEM and SAED patterns which showed nano-crystallinity in the micro environment of the sample. So we conclude that, the nanocomposites (both Set A and Set B) are overall amorphous in nature.

4.1.10. DLS measurement

Form DLS measurement we observed the hydrodynamic radii of the Set A and Set B were 615 nm and 396 nm respectively (Fig. 8). The apparently large deviation of size from that indicated by the TEM image is an obvious observation which occurs due to the enhanced hydrodynamic

radius in the solution phase of the particles in colloidal suspension [54] arising out of the prevailing hydration environment of the entities. The lower hydrodynamic radius of Set B as compared to Set A is due to the high energy gamma radiations which caused alterations in the hydration environment owing to the presence of free radicals in the medium. This is also in agreement with the trend observed in the TEM images.

4.2. XPS analysis:

XPS narrow scan spectra of Ru3d and C1s combined region (279 eV to 292 eV) of the nanocomposites (Set A and Set B) are shown in Fig.9. Ru3d region has significantly split spin-orbit components ($Ru3d_{5/2}$ and $Ru3d_{3/2}$) of 4.2 eV. Although C1s and Ru3d merges in this system, $Ru3d_{5/2}$ is outside C1s region and peak deconvolution of $Ru3d_{5/2}$ is not hindered by the presence of sp^2 hybridized C1s electrons. As shown in the Fig.9 A and B, both sets contain $RuCl_3$ and RuO_3. The atomic percentage of Ru in the form of $RuCl_3$ and RuO_3 are tabulated in Table 5 which reflects that radiolysis enhances the amount of RuO_3. This is a quite obvious observation as on radiolysis, lots of free radicals like $H^{\cdot}$ and $OH^{\cdot}$ are generated which augments the formation of RuO_3. The participation of morin in nanocomposite formation was verified by the peaks in the region of 284 to 288 eV which arise due to 1s orbital of sp^2 carbon, sp^3 carbon, C-O-C, C=O and carboxylic acid (-O-C=O). The atomic percentage of carbon in different chemical states (Table 6) also varied upon radiolysis. A prominent increase in the carbonyl content and sp^3 carbon content with associated decrease in the sp^2 carbon content clearly indicates the higher involvement of the polyphenol molecule towards nanocomposite formation. An internal molecular rearrangement is also indicated which boosts up the possibility of production of higher amounts of metallic oxide in the matrix. All these events result in the formation of a nanocomposite that has higher surface activity and is prone to show spectral changes in presence of selective analytes. The change of surface properties is in good agreement with the previous characterization methods and also with the concept of increase in surface activity towards sensing of lanthanides. The detail survey of the sensing properties is elaborated in the following section.

4.3. Sensing study

The sensing study was performed using absorption and emission spectroscopy. For the sensing experiment, lanthanoids viz., La(III), Ce(IV), Ce(III), Sm(III), Gd(III) and Dy(III) were taken each with concentration ~1 mM. The experiment was performed in three different pH solutions (2, 7 and 12). Only Set B was found to be capable of sensing Ce(IV), Ce(III) and Dy(III) of the chosen lanthanoids in contrast to Set A which did not show any spectral change under similar conditions. The mechanism behind such observation is described in the following section.

Upon addition of these metal solutions to that of the nanocomposite solution of Set B (varying pH) the absorbance value at a particular λ_{max} gradually increases for Ce(IV), Ce(III) and Dy(III). For other metal ions, the absorbance values decreases slightly only because of dilution effect which indicates that there were no prominent interactions between the individual metal ions and the nanocomposite solution.

From absorption spectral data, we observed that, Ce(IV) can be detected at all the experimental pH solutions. At pH 2 and pH 7, the characteristic peak of the nanocomposite is at ~293 nm. Upon interaction with Ce(IV), the absorbance value corresponding to the λ_{max} = 293 nm gradually increases (Fig. 10A and B respectively). The calibration plot of the same gives a straight line with a good coefficient of determination (R^2) (inset of Fig. 10 A and B). At pH 7 the linearity in the increasing absorbance at ~293 nm was observed in the range 2.37 to 11.74 µM concentration of Ce(IV). At pH 12, the characteristic peak of the nanocomposite itself was shifted to ~320 nm. In presence of low concentration of Ce(IV), the absorption value at ~320 nm increased gradually and the calibration plot gave a moderately good R^2 value (Fig. 10 C and its inset). The details of the parameters at all the three pH conditions are tabulated in Table 7.

We found that Ce(III) could only be detected at pH 12. The peak intensity of the nanocomposite solution at ~320 nm gradually increased on interaction with Ce(III). The calibration graph gives a straight line with a good coefficient of determination (R^2) (Fig. 10 D and its inset). The details of the analytical parameters and the limit of detection (LOD) are tabulated in Table 8.

For Dy(III), the effective pH was found to be pH 2. At this pH, the peak intensity of the nanocomposite solution gradually increased at λ_{max} = 293 nm upon interaction with low

concentration Dy(III) solution. A good calibration plot was obtained for this set also (Fig.11 A and its inset). The details of the analytical parameters are tabulated in Table 8.

Fluorimetric method also revealed a good sensing aptitude of the Set B solution towards Ce(IV) at pH 7. On excitation at λ_{ex} = 290 nm, the nanocomposite solution at pH 7 shows an emission band near ~391 nm. Upon addition of Ce(IV), the emission intensity gradually increases (Fig. 11 B). In order to compare the hike in emission intensity caused by the Ce(IV) solution in Set B and in blank solution (pH 7 solution only), we calculated the quantum yields (φ) for both of the processes. The result shows that the quantum yield for Ce(IV) in pH 7 – nanocomposite solution is higher (0.022) than that of Ce(IV) in pH 7 only (0.009). This confirms that, the increase in emission intensity is due to interaction between Ce(IV) and Set B. In other pHs (2 and 12), addition of little amount of Ce(IV) resulted in small and random changes in the emission intensity. This is because of the fact that at very low and high pH of the medium, the excess concentration of H^+ or OH^- ions causes a blocking in the emission pathway thereby making the optical environment inactive towards the analyte. Again, the increase in the emission intensity is guided by redox reactions and hence changes are observed only for the Ce(IV) species. The fluorescence emission remained unchanged with increasing additions of Ce(III) and Dy(III) as interactions with these ions are guided by other mechanism as is discussed in the "sensing mechanism".

Overall, it can be perceived that Set B solution has the potential for sensing Ce(IV) in pH 2, 7 and 12 using absorption spectral method and in pH 7 using fluorescence spectral method. Additionally, absorption spectral sensing of Ce(III) and Dy(III) is also possible by Set B in pH 12 and 2 respectively. Therefore, pH conditions provide mutually exclusive conditions for individual sensing of these three lanthanoid species in presence of one another. Ce(IV) can be assessed at low concentrations using pH 2 or 7 of Set B followed by analysis of Ce(III) at pH 12 which may have interference from Ce(IV). The amount of Ce(IV) obtained from pH 2 or 7 study may be subtracted to obtain the correct idea of Ce(III) concentration in a mixture. Similarly, correct analysis of Dy(III) at pH 2 is possible with a prior analysis of Ce(IV) at pH 7 or 12.

4.4. Sensing mechanism

It is evident from the characterization data (N_2 adsorption-desorption, TEM, DLS and XPS) that the effect of ionizing radiation causes some physicochemical changes of the nanocomposites. At

the same time, lots of free radicals and hydrated electrons are generated upon γ-irradiation. For these reasons surface of Set B becomes more active than Set A and is thus capable of sensing selected lanthanoids. Ce(IV), has a high reduction potential (1.72 V). This in combination with the fact that particles in Set B have higher surface activity makes it possible to reduce the ruthenium-morin nanocomposite and render observable absorption spectral changes in Set B solution at all the three pH conditions including emission spectral changes at pH 7. Ce(III) remains as $Ce(OH)_4^-$ in pH 12 medium. Therefore due to its high basicity it can donate its electron density to the ruthenium-morin nanocomposite and as a result the absorbance intensity is increased. At pH 2, the ruthenium-morin nanocomposites get protonated which results in a sterically crowded microenvironment prevailing in the medium. Dy(III) having a very high effective nuclear charge (8.85), the ionic radius of Dy(III) is very low which makes it fit to invade the sterically crowded environment and is therefore an eligible candidate to cause spectral changes in the γ-irradiated nanocomposite solution containing particles with high surface activity. Therefore, the lanthanoids capable to cause spectral changes interact with the microenvironment of the nanocomposite entities resulting in gradual increase in the effective particle size and correspondingly the band gap decreases (calculated from Tauc Plot) are reflected in Table 9. It was also experimentally verified that, neither γ-irradiated $RuCl_3$ nor γ-irradiated morin is capable of sensing any of the lanthanoids at any pH medium (Fig. S11 to Fig. S20).

The sensing mechanism was further strenghthened by the FTIR spectral analysis of the Set B nanocomposite and comparing it with that of the analyte treated nanocomposite. Fig. S21 represents the IR spectra of nanocomposite along with that of Ce(IV) treated nanocomposite at pH 2, 7 and 12. It is clear that the peaks in the region 1943-2061 cm^{-1} in the nanocomposite owing to the Ru-CO bond vibrations disappear in each of the Ce(IV) treated samples indicating probable oxidation. The aromatic C=C stretch (at pH 12) and -OH bending vibrations (at pH 2, 7 and 12) in Ce(IV) treated samples become prominent instead. Fig. S22 shows similar results for Ce(III) treated nanocomposite, where the Ru-CO bond vibration disappears due to electron donation by the $Ce(OH)_4^-$ moiety at pH 12. Fig. S23 shows a prominent vibrational peak at 1896 cm^{-1} owing to the terminal metal carbonyl bond vibration along with appearance of some free C=O stretching at 1701 cm^{-1}. This is mainly due to invasion of the small Dy(III) ions in the Ru-morin cage leading to the disruption of Ru-CO bond at some positions. Therefore, the IR spectra

support the interactions of the analyte molecules with the nanocomposite which are responsible for the observed sensing. The results with individual band identification are presented in Table S1.

4.5. Interference study

Interference from various other metal ions including transition metals and other lanthanoids were studied. The results are quite interesting and suggest that the Set B nanocomposite is selective towards sensing of the analyte in presence of other metal ions using absorption spectroscopy. The absorption spectrometric interference towards Ce(IV) (pH 2, 7, 12), Ce(III) (pH 12) and Dy(III) (pH 2) are shown in Fig. 12, 13 and 14 respectively. A similar emission spectrometric study for Ce(IV) shown in Fig. 15 shows no interference from other transition metals. However, prominent interferences were observed from some lanthanoids (La(III), Sm(III) and Gd(III)). This is due to the fact that emission is mostly affected by excited state interactions and lanthanoids having similar properties show similar behavior at their excited states and the sensing of the Ce(IV) gets affected. The absorption spectroscopy is free from such interference at similar conditions as only ground state interactions are observed in this method. Therefore in presence of other lanthanoids, absorption spectrometry is the preferred tool.

4.6. Analyses of environmental samples

To check the practicability of the developed method, two environmental samples, tap water and ground water were analyzed for their Ce(IV), Ce(III) and Dy(III) recovery using Set B samples. Considering the values of their LOD and the experimental conditions, the absorption spectrometric analyses were performed at pH 2, 7 and 12 for Ce(IV), pH 12 for Ce(III) and at pH 2 for Dy(III). Neither of the samples showed measurable amounts of lanthanoid species using the Set B nanocomposite solution. In order to examine the recovery percentage of the lanthanoids, we added some measured aliquots of the respective species externally and observed significant recovery could be done from majority of the conditions. However, at basic pH of ground water, analysis of Ce(III) could not be performed satisfactorily which is due to hydroxide precipitation of the excessive dissolved minerals present in it (data not shown). Overall the recovery at pH 12

was not as precise as in lower pHs. Therefore, analysis of environmental samples at low to neutral pH is recommended.

5. Conclusion

In this work two sets of ruthenium-morin nanocomposites have been prepared in presence and in absence of γ-irradiation. The particle size of these nanocomposites lie in the range of 15 to 20 nm and pore size lie in the mesoporous range. Only the γ-irradiated nanocomposite is capable of sensing of Ce(IV), Ce(III) and Dy(III) out of the different lanthanoid species (viz., La(III), Ce(IV), Ce(III), Sm(III), Gd(III) and Dy(III)) at different pH media. It is possible to detect all the three lanthanoid species at micromolar concentration range using simple spectroscopic methods. The pH conditions may be optimized for mutually exclusive analysis of all the three individual ions Ce(IV), Ce(III) and Dy(III) in presence of one another using the γ-irradiated nanocomposite. The absorption spectrophotometric analysis also suggested that neither the examined transition metals nor the lanthanoids make any significant interference in the analyses. A significant interference was however observed from lanthanoids when analysed fluorimetrically. This may be due to excited state interactions between the reacting entities prevailing during fluorimetry. On analysis of environmental samples we observed significant recovery of Ce(IV), Ce(III) and Dy(III) from tap water and Ce(IV) and Dy(III) from ground water at low to neutral pH. Therefore, the method can be designated as a simple and yet promising for selective low concentration detection and analysis of the chosen lanthanoid ions (Table 1).

Acknowledgement

Pritam Singh gratefully acknowledges the University Grants Commission (UGC) (Ref. No. 20/12/2015(ii)EU-V dated 24.08.2016) for providing necessary fellowship. We are also grateful to Dr. Abhijit Saha, Centre Director, and Dr (Ms.) Aparna Datta, Scientific Assistant-F, UGC-DAE Consortium for Scientific Research, Kolkata Centre for performing the fluorescence spectroscopy and the gamma irradiation at their centre. We also express our sincere gratitude to Mr. Nayan Ranjan Saha, Department of Chemical Technology, University of Calcutta, India for measuring the XRD analysis.

References

[1] A. Dikhtiarenko, S. A. Khainakov, O. Khaynakova, J. R. García, J. Gimeno, High-yielding green hydrothermal synthesis of ruthenium nanoparticles and their characterization, J. Nanosci. Nanotechnol., 16 (2016) 6139-6147.

[2] S. K. Kannan, M. Sundrarajan, Green synthesis of ruthenium oxide nanoparticles: Characterization and its antibacterial activity, Adv. Powder Technol., 26 (2015) 1505-1511.

[3] B. Thirumalraja, C. Rajkumara, S-M Chen, P. Veerakumar, P. Perumal, S-B Liu, Carbon aerogel supported palladium-ruthenium nanoparticles for electrochemical sensing and catalytic reduction of food dye, Sens. Actuators B, 257 (2018) 48-59.

[4] L. Wand, R. T. Yang, Hydrogen storage properties of carbons doped with ruthenium, platinum, and nickel nanoparticles, J. Phys. Chem. C 112 (2008) 12486-12494.

[5] T. D. Thangadurai, K. Natarajan, Antibacterial activity of ruthenium(II) carbonyl complexes containing tetradentate Schiff bases, Transit. Metal Chem., 27 (2002) 485-489.

[6] V. Kruefu, A. Wisitsoraat, D. Phokharatkul, A. Tuantranont, S. Phanichphant, Enhancement of p-type gas-sensing performances of NiO nanoparticles prepared by precipitation with RuO_2 impregnation, Sens. Actuators B, 236 (2016) 466-473.

[7] Z. Yu-qing, C. Xi, W. De-jun, A magnetic mesoporous nanocomposite modified with a ruthenium complex for site-specific molecular oxygen sensing: construction and characterization, Opt. Mater., 46 (2015) 393-400.

[8] A. Salomonsson, R. M. Petoral Jr., K. Uvdal, C. Aulin, P-O. Käll, L. Ojamäe, M. Strand, M. Sanati, A. L. Spetz, Nanocrystalline ruthenium oxide and ruthenium in sensing applications – An experimental and theoretical study, J. Nanoparticle Res., 8 (2006) 899-910.

[9] Z. Jiang, X. Yu, S. Zhai, Y. Hao, Ratiometric dissolved oxygen sensors based on ruthenium complex doped with silver nanoparticles, Sensors, 17 (2017) 548-564.

[10] Y. Li, Z. Hua, Y. Wu, Y. Zeng, Z. Qiu, X. Tian, M. Wang, E. Li, Modified impregnation synthesis of Ru-loaded WO_3 nanoparticles for acetone sensing, Sens. Actuators B, 265 (2018) 249-256.

[11] K-H Kim, S-J Kim, H-J Cho, N-H Kim, J-S Jang, S-J Choi, I-D Kim, WO_3 nanofibers functionalized by protein-templated RuO_2 nanoparticles as highly sensitive exhaled breath gas sensing layers, Sens. Actuators B, 241 (2017)1276-1282.

[12] X. Ni, B. Zhang, C. Li, M. Pang, D. Su, C. T. Williams, C. Liang, Microwave-assisted green synthesis of uniform Ru nanoparticles supported on non-functional carbon nanotubes for cinnamaldehyde hydrogenation, Catal. Commun., 24 (2012) 65-69.

[13] J. Zhao, W. Hu, H. Li, M. Ji, C. Zhao, Z. Wang, H. Hu, One-step green synthesis of aruthenium/graphene composite as a highly efficient catalyst, RSC Adv., 5 (2015) 7679-7686.

[14] Z. Ansari, S. Dhara, B. Bandyopadhyay, A. Saha, K. Sen, Spectral anion sensing and γ-radiation induced magnetic modifications of polyphenol generated Ag-nanoparticles, Spectrochim. Acta A: Molecular and Biomolecular Spectroscopy, 156 (2016) 98-104.

[15] I. V. Korolkov, A. A. Mashentseva, O. Güven, Y. G. Gorin, A. L. Kozlovskiy, M. V. Zdorovets, I. S. Zhidkov, S. O. Cholach, Electron/gamma radiation-induced synthesis and catalytic activity of gold nanoparticles supported on track-etched poly(ethylene terephthalate) membranes, Mater. Chem. Phys., 217 (2018) 31-39.

[16] A. C. Dhayagude, A. Das, S. S. Joshi, S. Kapoor, γ-Radiation induced synthesis of silver nanoparticles in aqueous poly (N-vinylpyrrolidone) solution, Colloids Surf. A: Physicochem. Eng. Aspects, 556 (2018) 148-156.

[17] K. Roy, S. Lahiri, A green method for synthesis of radioactive gold nanoparticles, Green Chem., 8 (2006) 1063-1066.

[18] S-M Kang, C. H. Kwak, M. Rethinasabapathy, S-C. Jang, S-R. Choe, C. Roh, Y-K. Han, Y. S. Huh, Gamma radiation mediated green technology for Pd nanoparticles recovery from waste water, Sep. Purif. Technol., 197 (2018) 220-227.

[19] O. M. Andersen, K. R. Markham, Flavonoids: Chemistry, biochemistry and applications, CRC Press, Published December 9, 2005, ISBN 9780849320217 - CAT# 2021.

[20] Q. K. Panhwar, S. Memon, Synthesis of Cr(III)-morin complex: Characterization and antioxidant study, Hindawi Publishing Corporation, Sci. World J., 2014.

[21] G. I. Vargas-Zúñiga, J. L. Sessler, The rare earth elements, Edited by David A. Atwood., ISBN 978-1-119-95097-4.

[22] A. I. Medalia, B. J. Byrne, Spectrophotometric determination of cerium(IV), 23 (1951) 453-456.

[23] V. K. Gupta, A. K. Singh, B. Gupta, A cerium(III) selective polyvinyl chloride membrane sensor based on a Schiff base complex of N,N′-bis[2-(salicylideneamino)ethyl]ethane-1,2-diamine, Anal. Chim. Acta, 575 (2006) 198-204.

[24] K. Matharu, S. K. Mittal, S. K. A. Kumar, Conductometric performance of two-pole and five-ring conductivity cell probes for lanthanide determination using EDTA and DCTA as potential sequestering agents, Ind. Eng. Chem. Res., 51 (2012) 11328−11334.

[25] M. N. Church, J. D. Spear, R.E. Russo, G. L. Klunder, P.M. Grant, B. D. Andresen, Transient isotachophoretic-electrophoretic separations of lanthanides with indirect laser-induced fluorescence detection, Anal. Chem., 70 (1998) 2475-2480.

[26] S. S. M. Hassan, W. H. Mahmoud, Spectrophotometric, potentiometric, and gravimetric determination of lanthanides with *peri*-dihydroxynaphthindenone, Anal. Chem., 54 (1982) 228-231.

[27] M. R. Ganjali, J. Ravanshad, M. Hosseini, M. Salavati-Niasari, M. R. Pourjavid, M. R. Baezzat, Novel Dy(III) sensor based on a new bis-pyrrolidene schiff's base, Electroanalysis, 16 (2004) 1771-1776.

[28] M. R. Ganjali, R. Zare-Dorabei, P. Norouzi, Design and construction of a novel optical sensor for determination of trace amounts of dysprosium ion, Sens. Actuators B, 143 (2009) 233-238.

[29] A. L. Jenkins, G. M. Murray, Ultratrace Determination of selected lanthanides by luminescence enhancement, Anal. Chem., 68 (1996) 2974-2980.

[30] F. J. Gustafson, J. C. Wright, Trace analysis of lanthanides by laser excitation of precipitates, Anal. Chem., 51 (1979) 1762-1774.

[31] I. N. Izosimov, N. G. Firsin, N. G. Gorshkov, S. N. Nekhoroshkov, Detection of lanthanides and actinides in solutions based on laser-induced luminescence and chemiluminescence, Hyperfine Interact., 227 (2014) 271-281.

[32] M. R. Buchmeiser, G. Seeber, R. Tessadri, Quantification of lanthanides in rocks using succinic acid-derivatized sorbents for on-line SPE-RP-ion-pair HPLC, Anal. Chem., 72 (2000) 2595-2602.

[33] N. Öztekin, F. B. Erim, Separation and direct UV detection of lanthanides complexed with cupferron by capillary electrophoresis, J. Chromatogr. A, 865 (2000) 263-268.

[34] H. G. Brittain, Submicrogram determination of lanthanides through quenching of calcein blue fluorescence, Anal. Chem., 59 (1987) 1122-1125.

[35] Z. Ansari, K. Sarkar, A. Saha, A. Singha, K. Sen, Enhanced anion sensing by γ-irradiated polyphenol capped iron oxide nanoparticles, J. Radioanal. Nucl. Chem., 308 (2016) 517-525.

[36] A. Blainski, G. C. Lopes, J. C. P. de Mello, Application and analysis of the folin ciocalteu method for the determination of the total phenolic content from Limoniumbrasiliense L., Molecules, 18 (2013) 6852-6865.

[37] E. A. Ainsworth, K. M. Gillespie, Estimation of total phenolic content and other oxidation substrates in plant tissues using folin–ciocalteu reagent, Nat. Protoc., 2 (2007) 875-877.

[38] A. Daneshfar, H. S. Ghaziaskar, N. Homayoun, Solubility of gallic acid in methanol, ethanol, water, and ethyl acetate, J. Chem. Eng. Data, 53 (2008) 776–778.

[39] C. V. Banks, J. W. O'laughlin, Spectrophotometric determination of ruthenium with 1,10-phenanthroline, Anal. Chem., 29 (1957) 14212-1417.

[40] M-C Daniel, D. Astruc, Gold nanoparticles: assembly, supramolecular chemistry, quantum-size-related properties, and applications toward biology, catalysis, and nanotechnology, Chem. Rev., 104 (2004) 293–346.

[41] S. K. Ghatak, D. Dey, S. Sen, K. Sen, Aromatic amino acids in high selectivity bismuth(III)recognition, Analyst, 138 (2013) 2308–2314.

[42] N. T. K. Thanh, N. Maclean, S. Mahiddine, Mechanisms of nucleation and growth of nanoparticles in solution, Chem. Rev., 114 (2014) 7610−7630.

[43] Z. Ansari, S. S. Singha, A. Saha, K. Sen, Hassle free synthesis of nanodimensional Ni, Cu and Zn sulfides for spectral sensing of Hg, Cd and Pb: A comparative study, Spectrochim. Acta A: Molecular and Biomolecular Spectroscopy, 176 (2017) 67-78.

[44] P. Singh, K. Sen, Drug delivery of sulphanilamide using modified porous calcium carbonate, Colloid Polym. Sci., 296 (2018) 1711-1718.

[45] S-S. Chang, B. Clair, J. Ruelle, J. Beauchêne, F. Di Renzo, F.Quignard, G-J. Zhao, H. Yamamoto, J. Gril, Mesoporosity as a new parameter for understanding tension stress generation in trees, J. Exp. Bot., 60 (2009) 3023-3030.

[46] L. Samet, K. March, N. Brun, F. Hosni, O. Stephan, R. Chtourou, Effect of gamma radiation on the photocatalytic properties of Cu doped titania nanoparticles, Mater. Res. Bull., 107 (2018) 1-7.

[47] K. D. N. Vo, C. Kowandy, L. Dupont, X. Coqueret, N. Q. Hien, Radiation synthesis of chitosan stabilized gold nanoparticles comparison between e^- beam and γ irradiation, Radiat. Phys. Chem., 94 (2014) 84-87.

[48] N. K. Fuloria, S. Fuloria, Spectroscopy: fundamentals and data interpretation, ISBN-10: 9380012586, ISBN-13: 978-9380012582, Publisher; Studium Press India Pvt. Ltd., Year: 2013.

[49] M. P. Shah, Exploited application of lactobacillus in microbial degradation and decolorization of acid orange, IJEBB, 2 (2014) 160-166.

[50] C. Stammer, A. Taurins, Infrared spectra of phenazines, Spectrochim. Acta, 19 (1963) 1625-1653.

[51] A. S. Gilbert, IR spectral group frequencies of organic compounds, Academic Press, 1035-1048.

[52] N. M. Logacheva, V. E. Baulin, A. Yu. Tsivadze, E. N. Pyatova, I. S. Ivanova, Y. A. Velikodny, V. V. Chernyshev, Ni(II), Co(II), Cu(II), Zn(II) and Na(I) complexes of a hybrid ligand 4'-(4'''-benzo-15-crown-5)-methyloxy-2,2':6',2''-terpyridine, Dalton Trans., 0 (2009) 2482–2489.

[53] R. A. Yadav, V. Dixit, M. Yogesh, C. Santhosh, Raman and IR spectral and DFT based vibrational and electronic characterization of isolated and zwitterionic forms of L-tyrosine, Pharm. Anal. Acta., 6 (2015) 1-18.

[54] Z. Ansari, A. Saha, S. S. Singha, K. Sen, Phytomediated generation of Ag, CuO and Ag-Cu nanoparticles for dimethoate sensing, J. Photochem. Photobiol A: Chemistry, 367 (2018) 200-211.

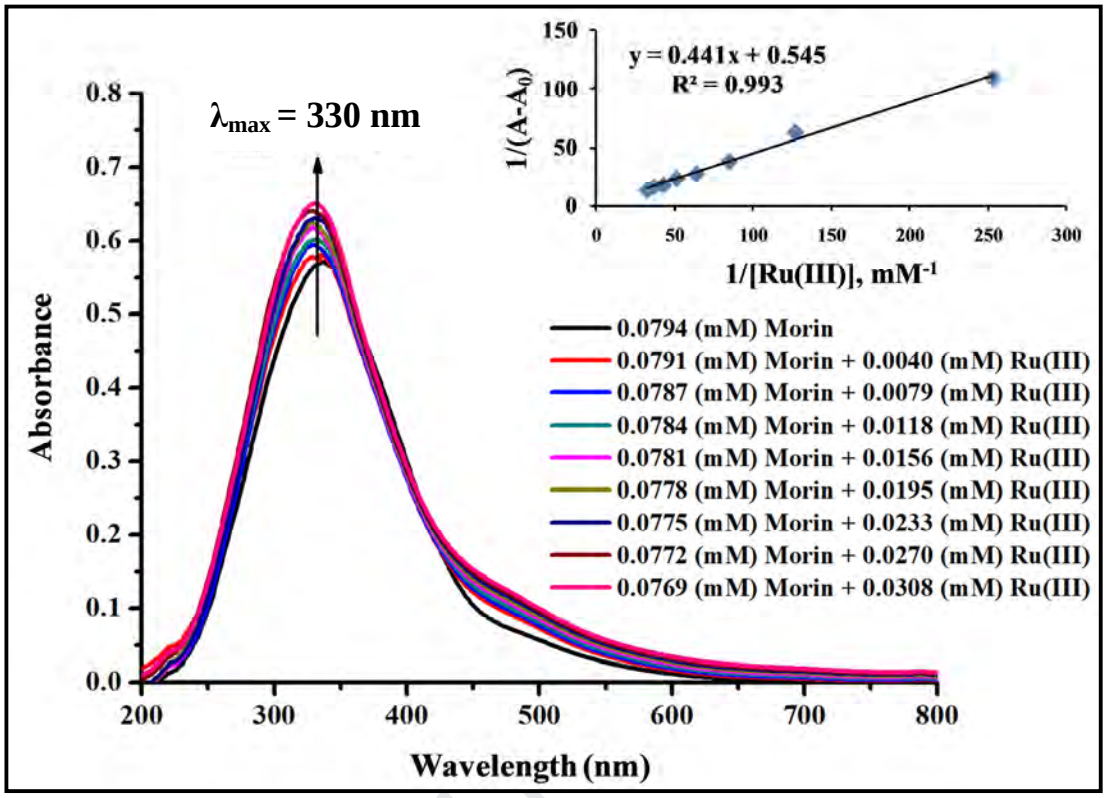

Fig. 1. UV interaction data and B-H plot (inset) between morin and ruthenium at pH 12.

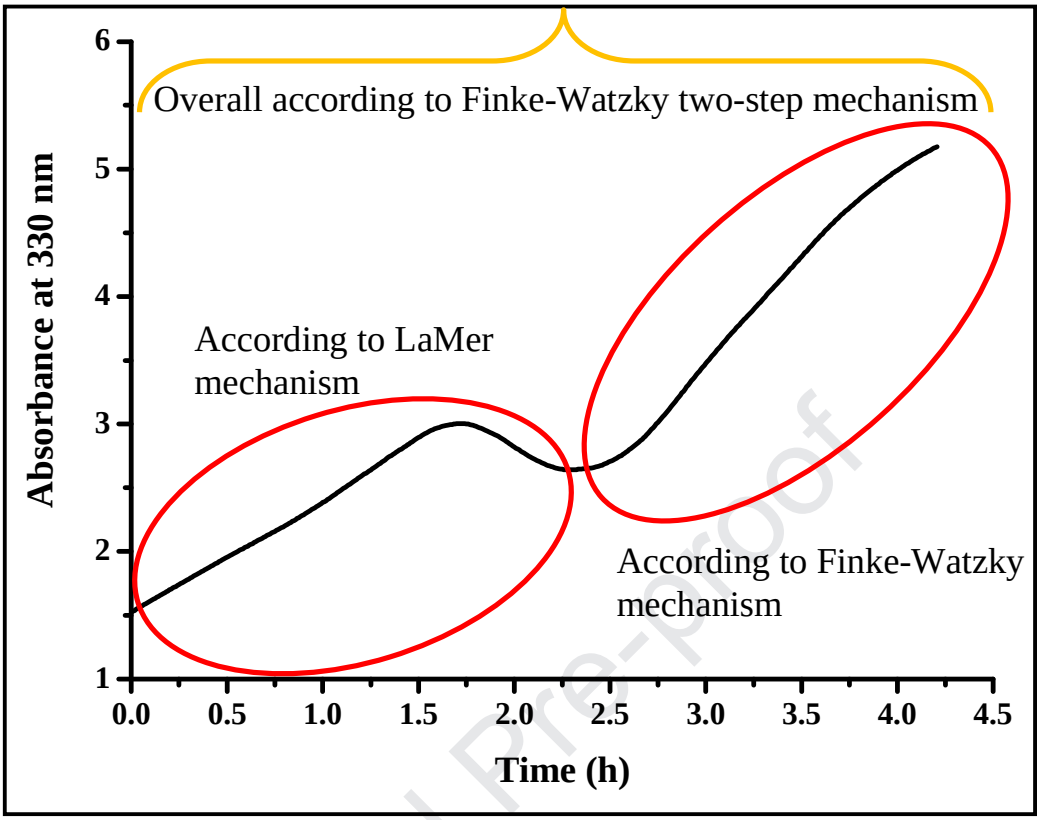

Fig. 2. Time scan profile for Ru-Morin nanocomposite at pH 12.

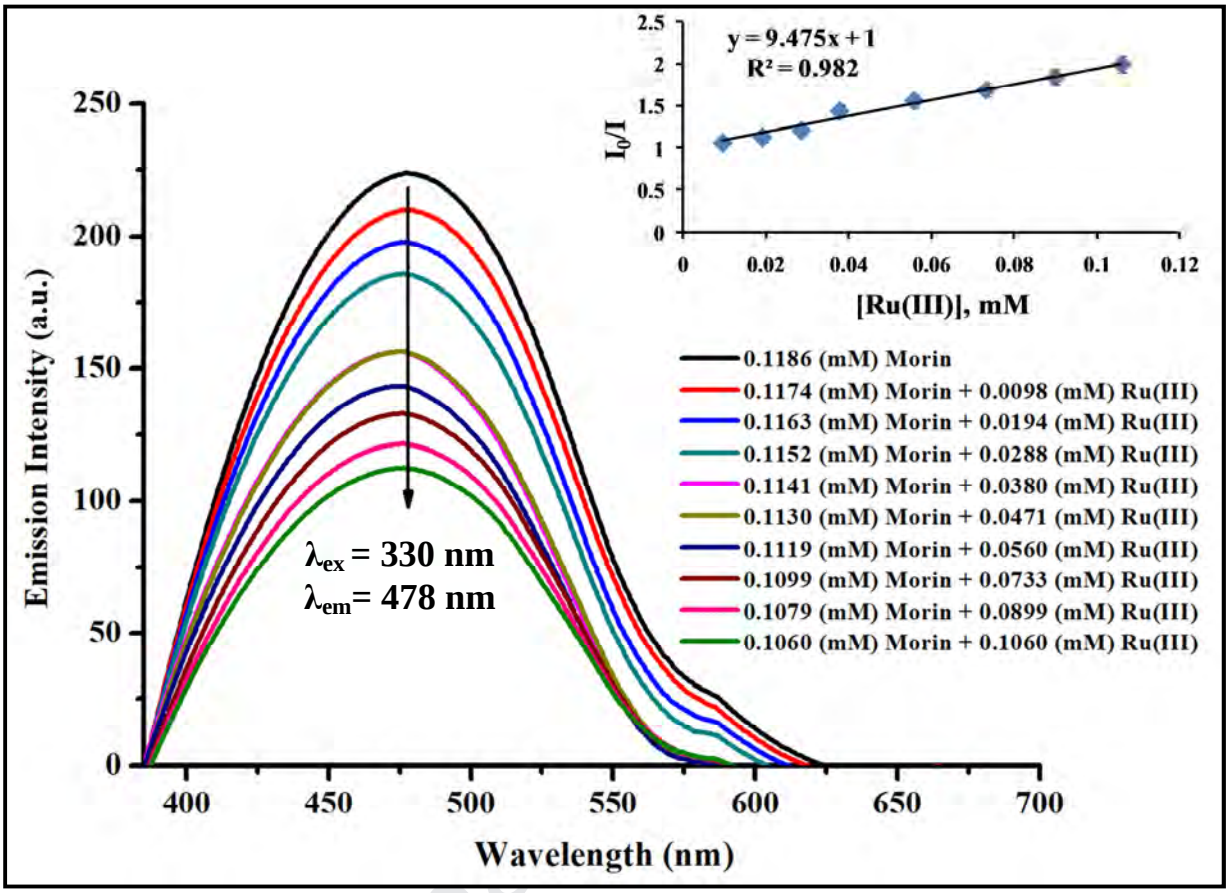

Fig. 3. Fluorimetric interaction data and S-V plot (inset) between morin and ruthenium at pH 12.

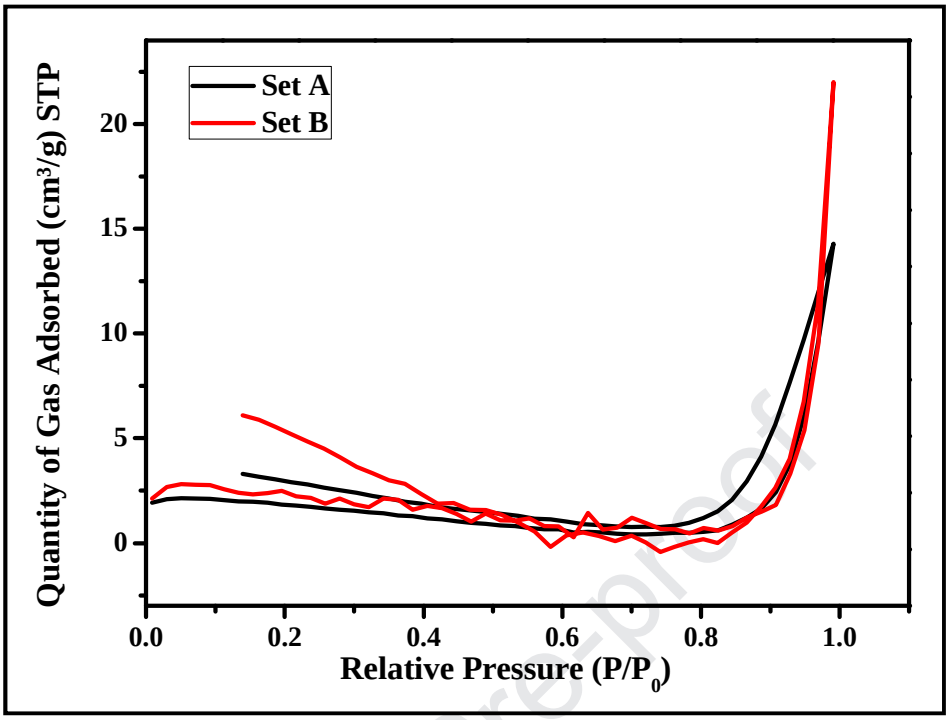

Fig. 4. N_2 adsorption-desorption isotherm of Set A and Set B nanocomposites.

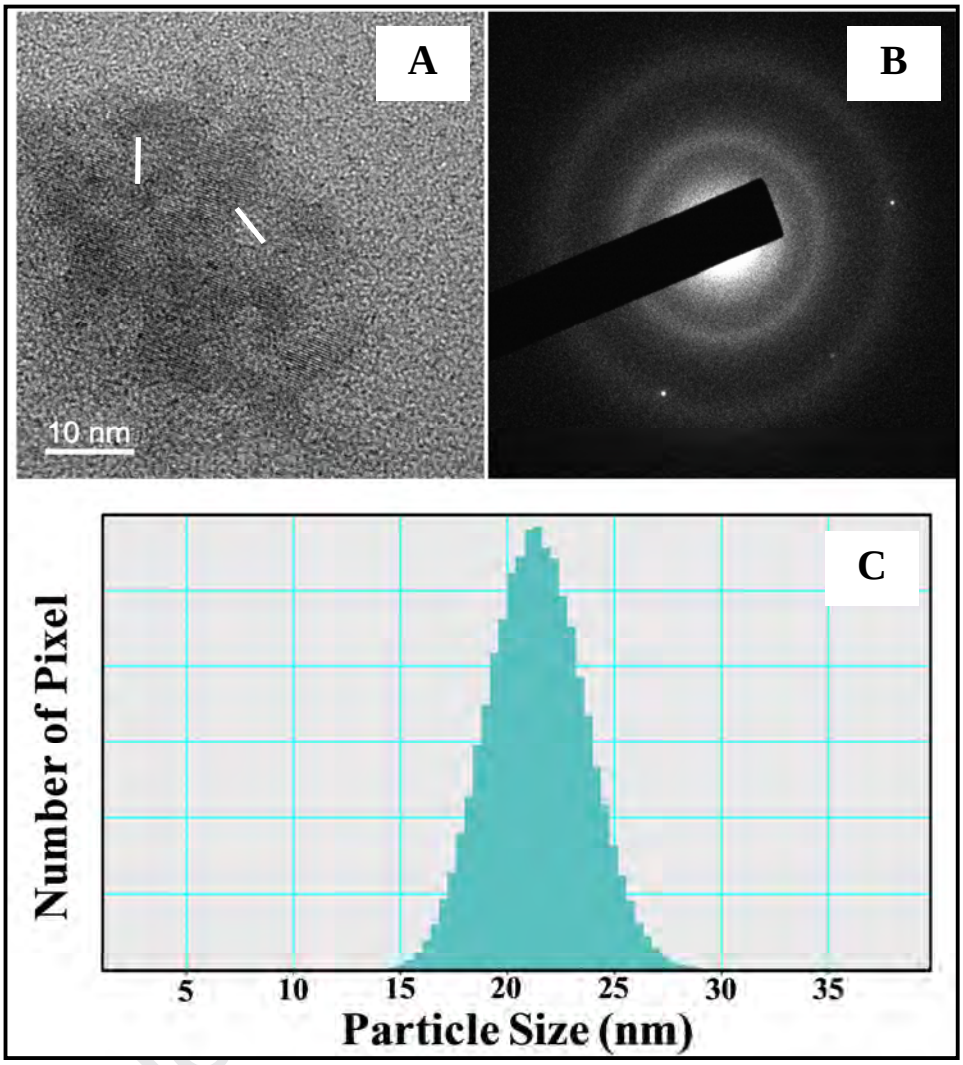

Fig. 5. A) TEM image, B) SAED pattern and C) Histogram of Set A nanocomposite.

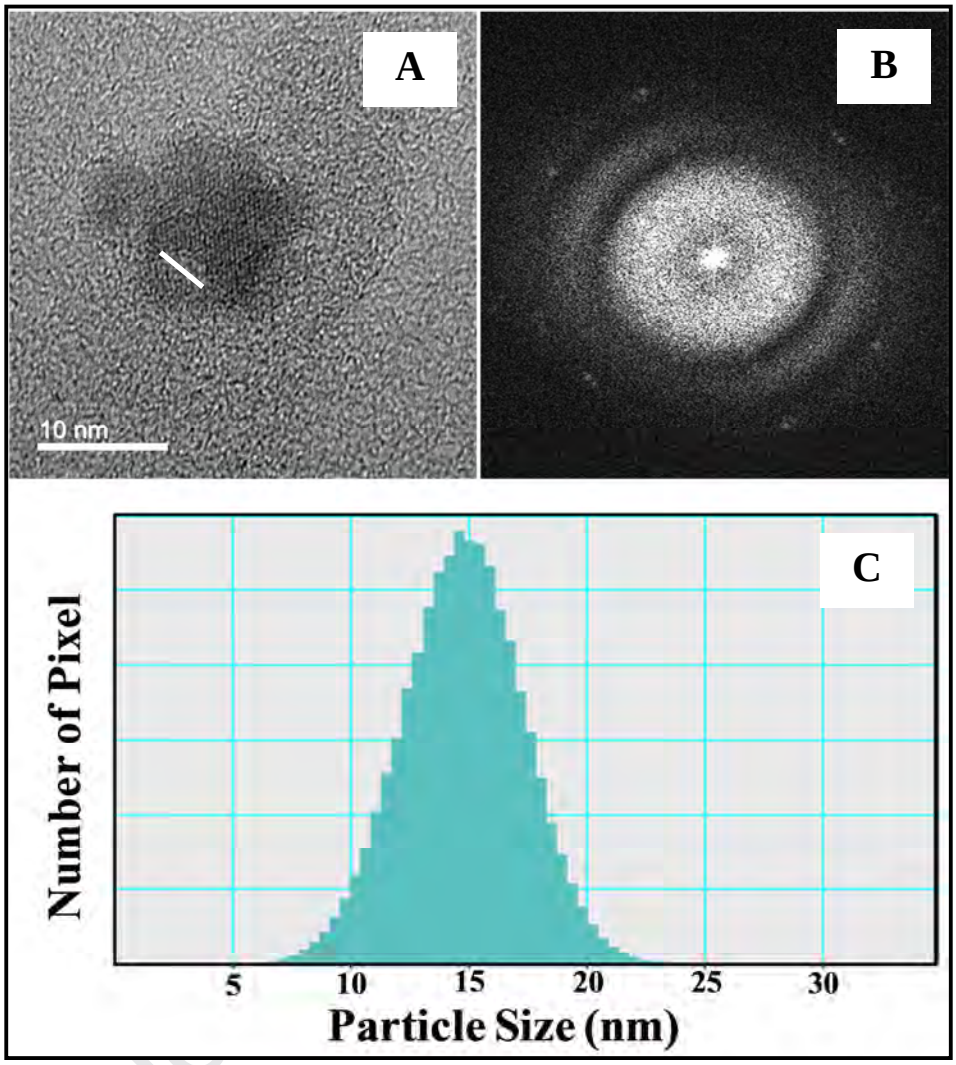

Fig. 6. A) TEM image, B) SAED pattern and C) Histogram of Set B nanocomposite.

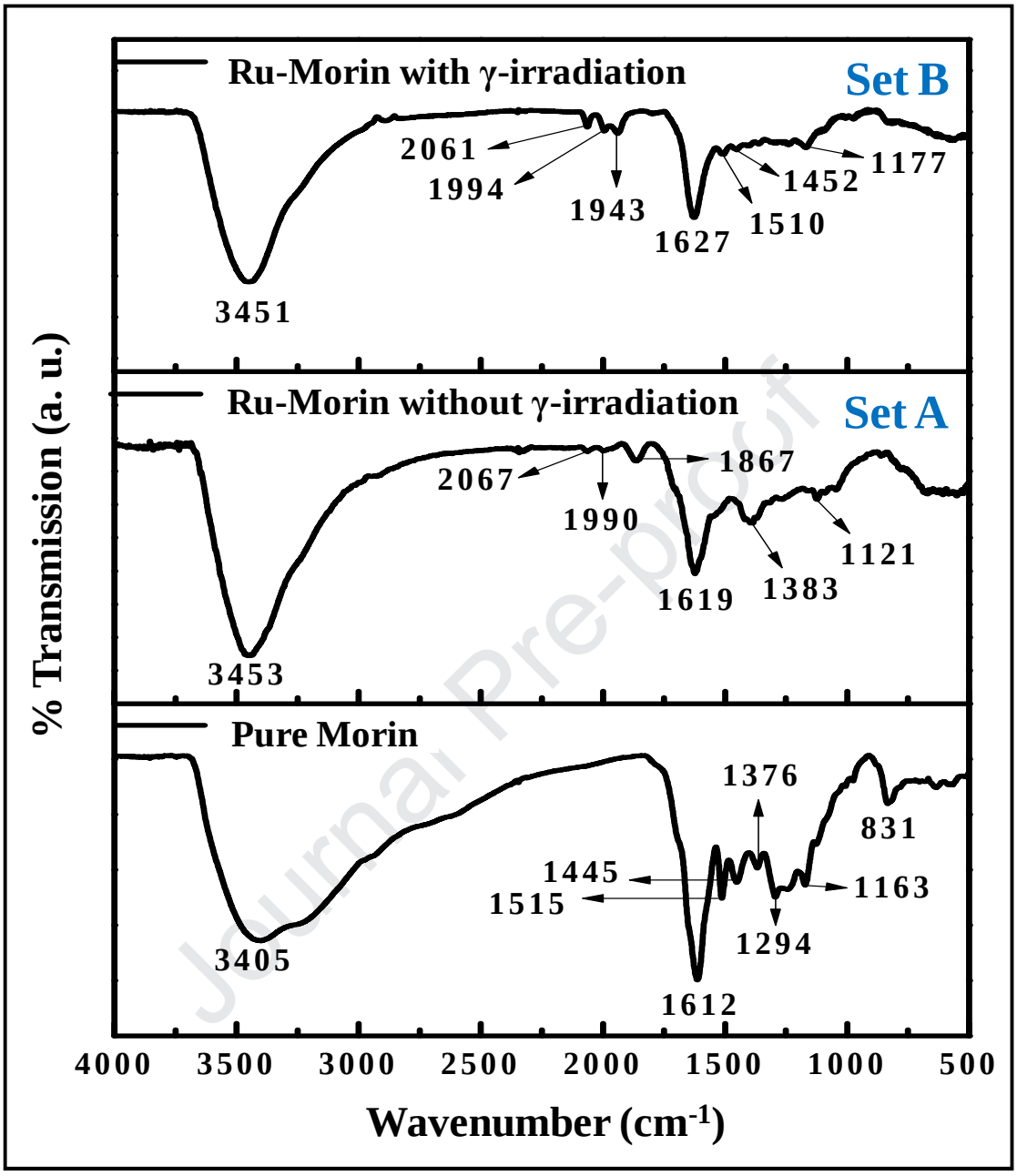

Fig. 7. FTIR spectra of pure morin, Set A and Set B nanocomposite.

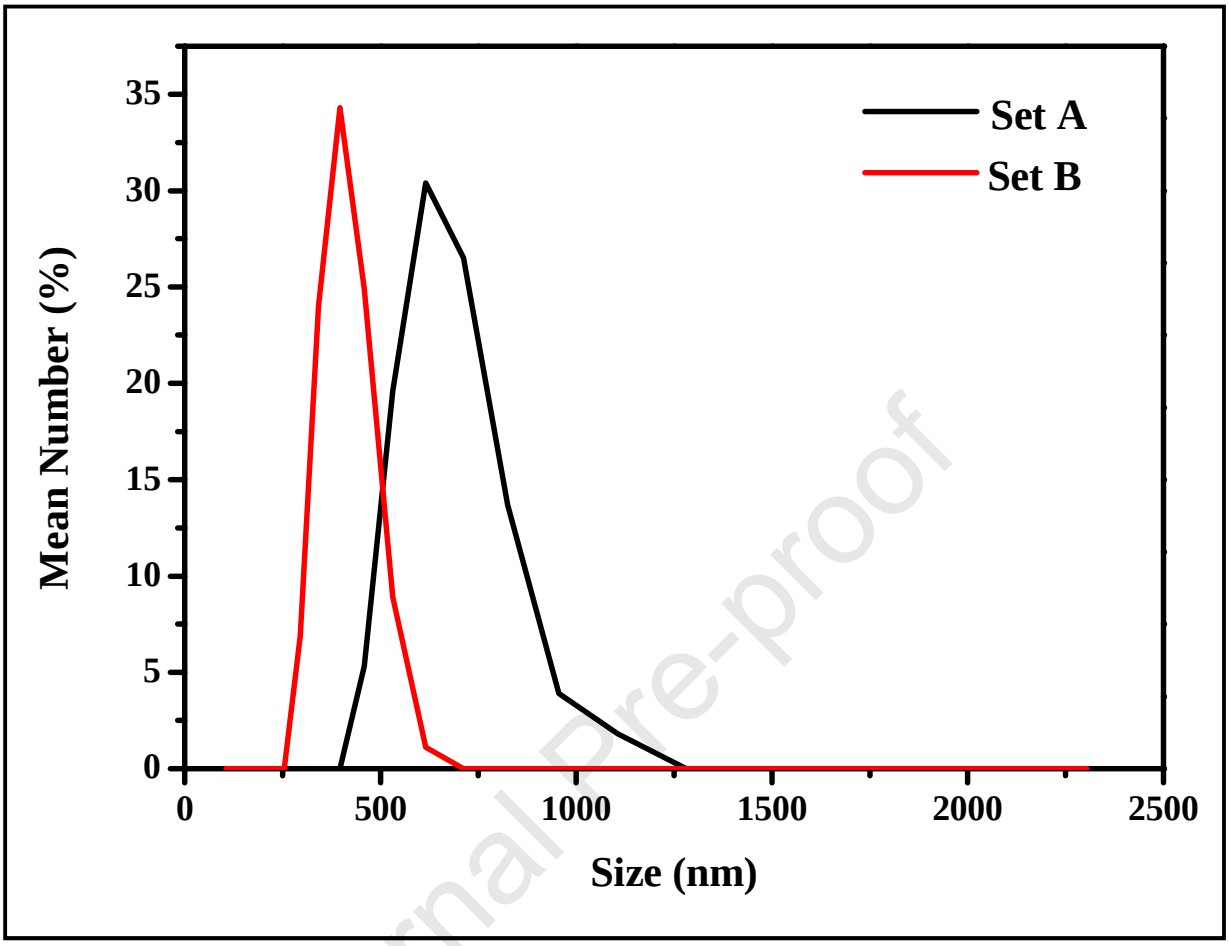

Fig. 8. DLS measurement of Set A and Set B nanocomposite.

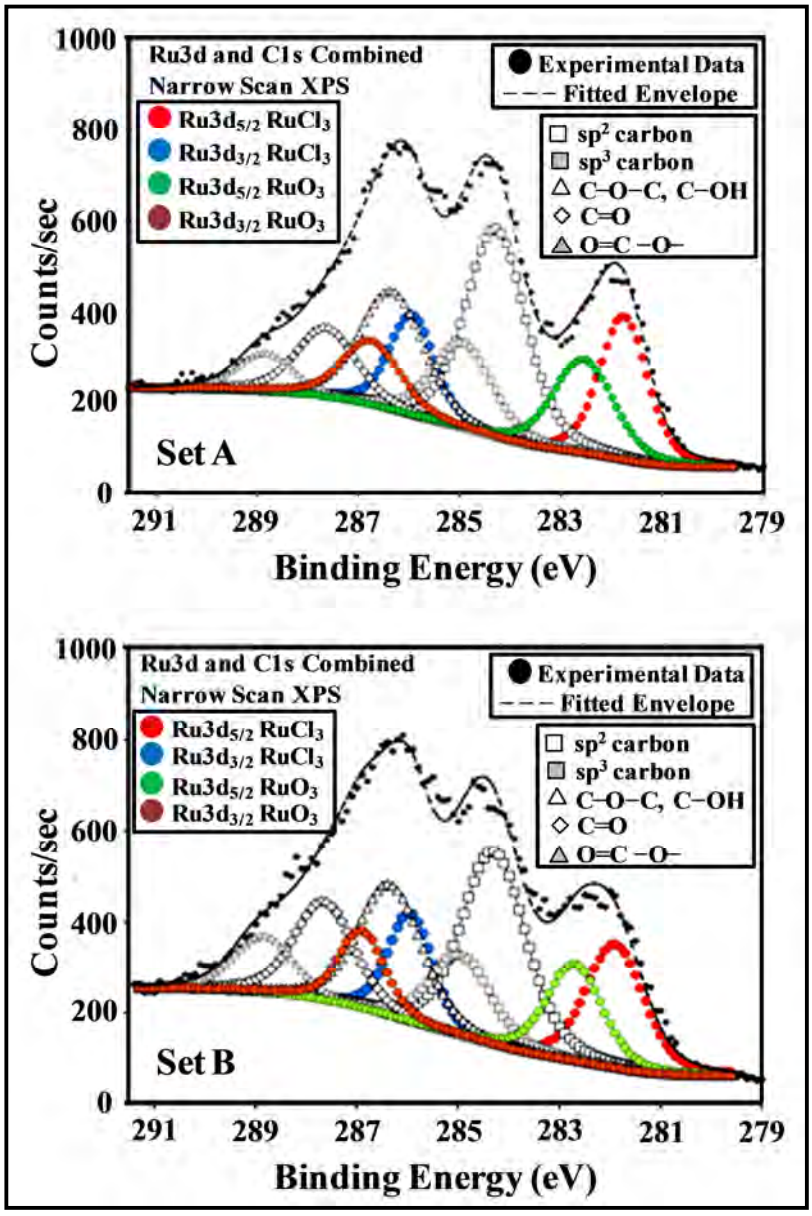

Fig. 9. Example XPS narrow scan data of overlapped C1s and Ru3d of Set A and Set B nanocomposite. Peak deconvolution shows the increase in RuO_3 when nano particles are prepared under gamma radiation. All peaks were assigned following NIST XPS reference database and symbols used for each assignment are shown.

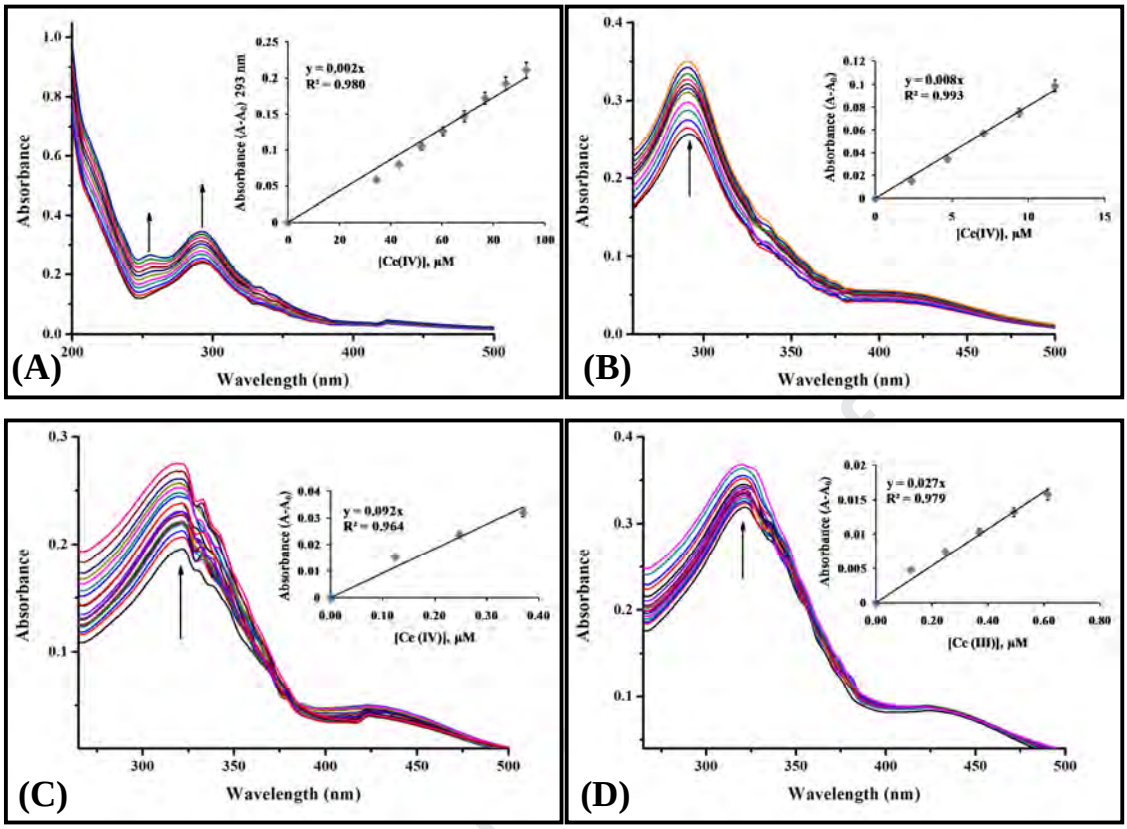

Fig. 10. Absorption spectral changes of Set B nanocomposite solution upon treatment with low concentration Ce(IV) solution at (A) pH 2 (λ_{max} = 293 nm), (B) pH 7 (λ_{max} = 293 nm), (C) pH 12 (λ_{max} = 320 nm) and (D) with low concentration Ce(III) solution at pH 12 (λ_{max} = 320 nm).

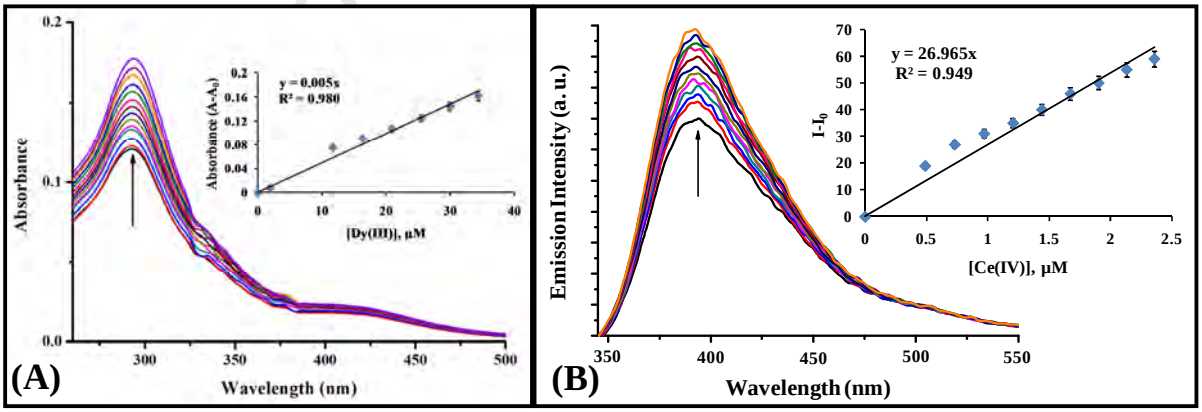

Fig. 11. (A) Absorption spectral changes of Set B nanocomposite solution upon treatment with low concentration Dy(III) solution at pH 2 (λ_{max} = 293 nm). And (B) emission spectral changes of Set B nanocomposite solution upon treatment with low concentration Ce(IV) solution at pH 7 (λ_{ex} = 290 nm, λ_{em} = 391 nm).

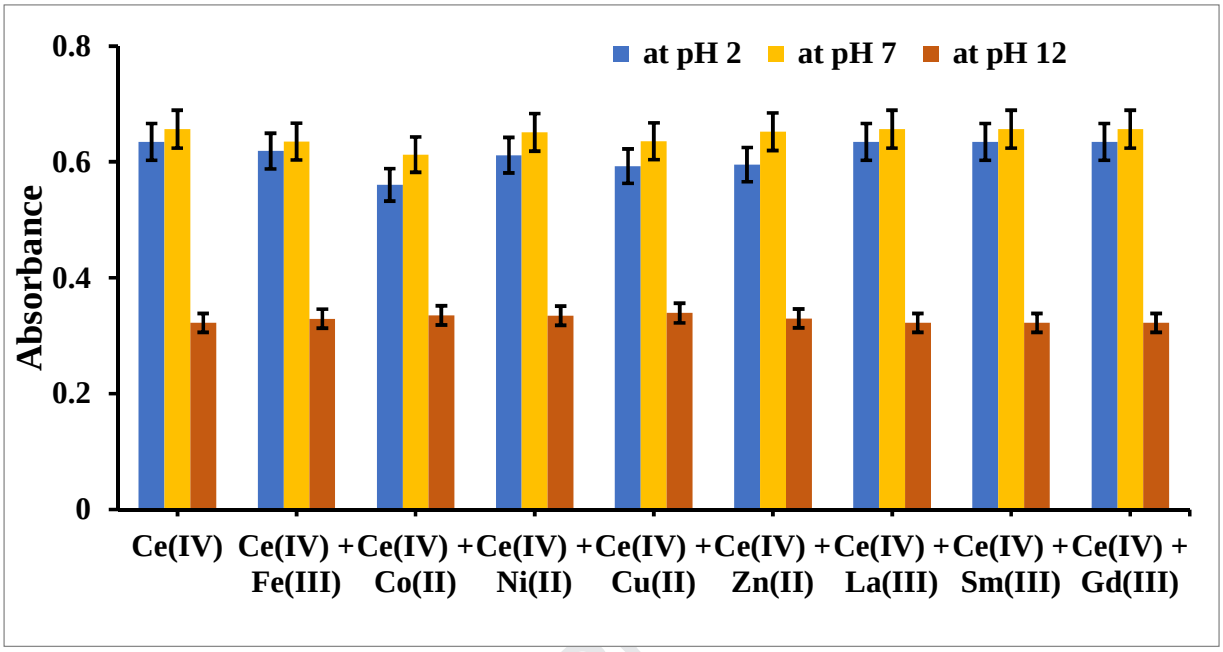

Fig. 12. Effect of interference from equimolar concentration of other metal ions towards Ce(IV) detection at pH 2 (45 µM each), pH 7 (9.7 µM each) and pH 12 (0.49 µM each).

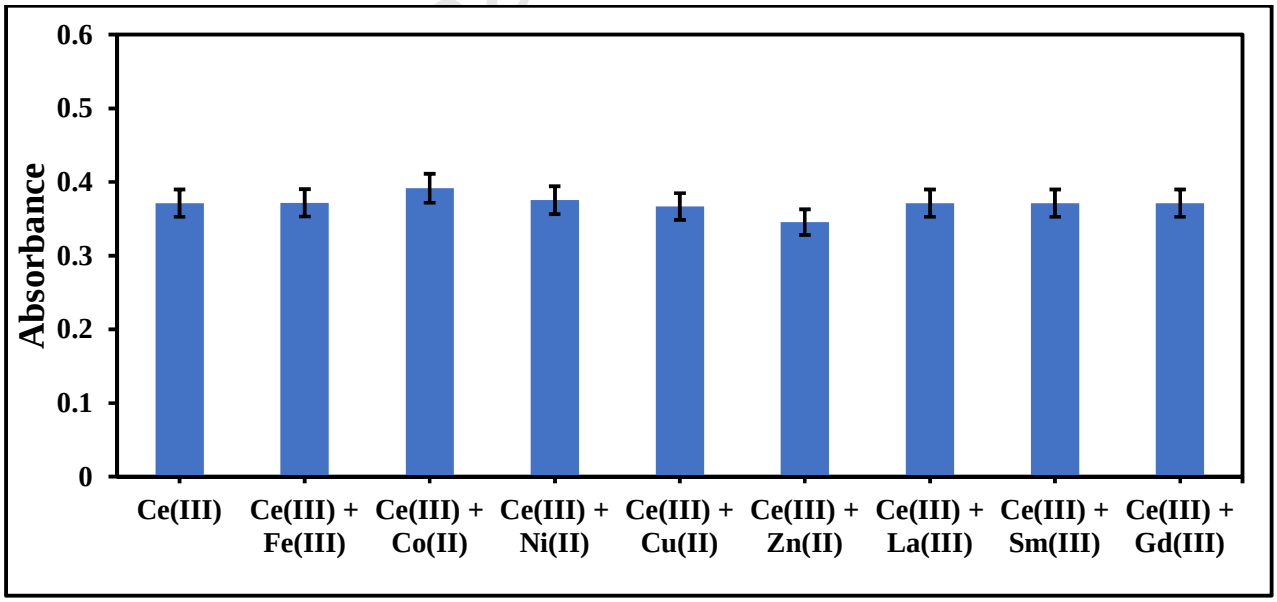

Fig. 13. Effect of interference from equimolar concentration of other metal ions towards Ce(III) detection at pH 12 (0.49 µM each).

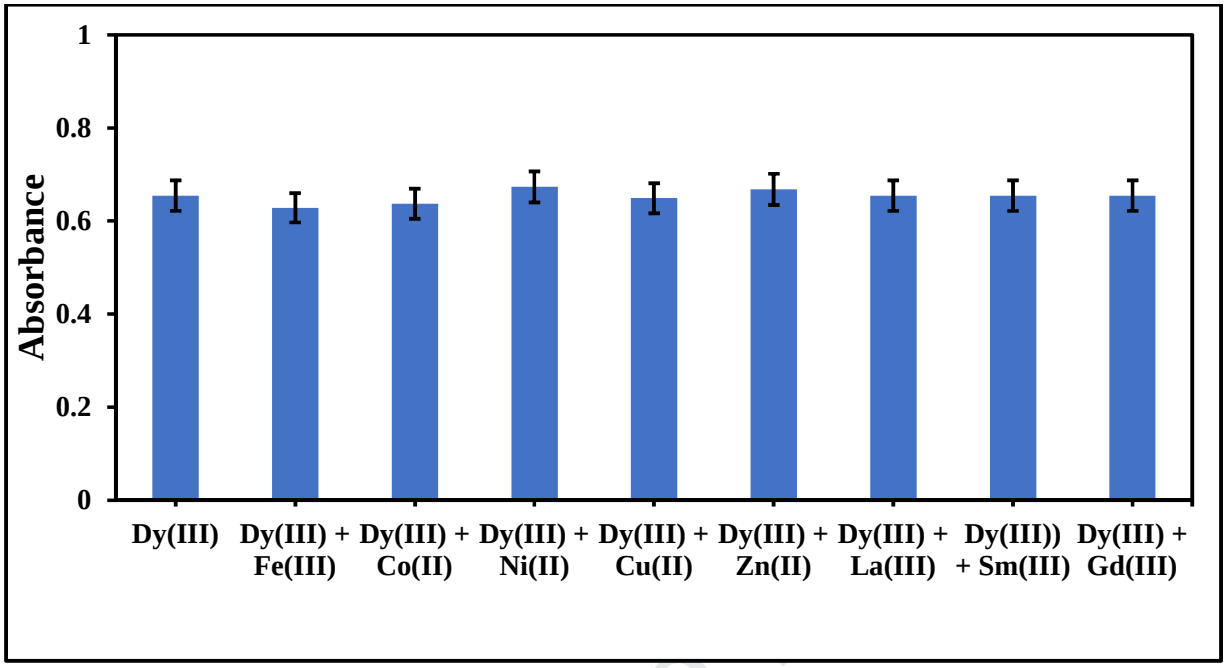

Fig. 14. Effect of interference from equimolar concentration of other metal ions towards Dy(III) detection at pH 2 (19 µM each).

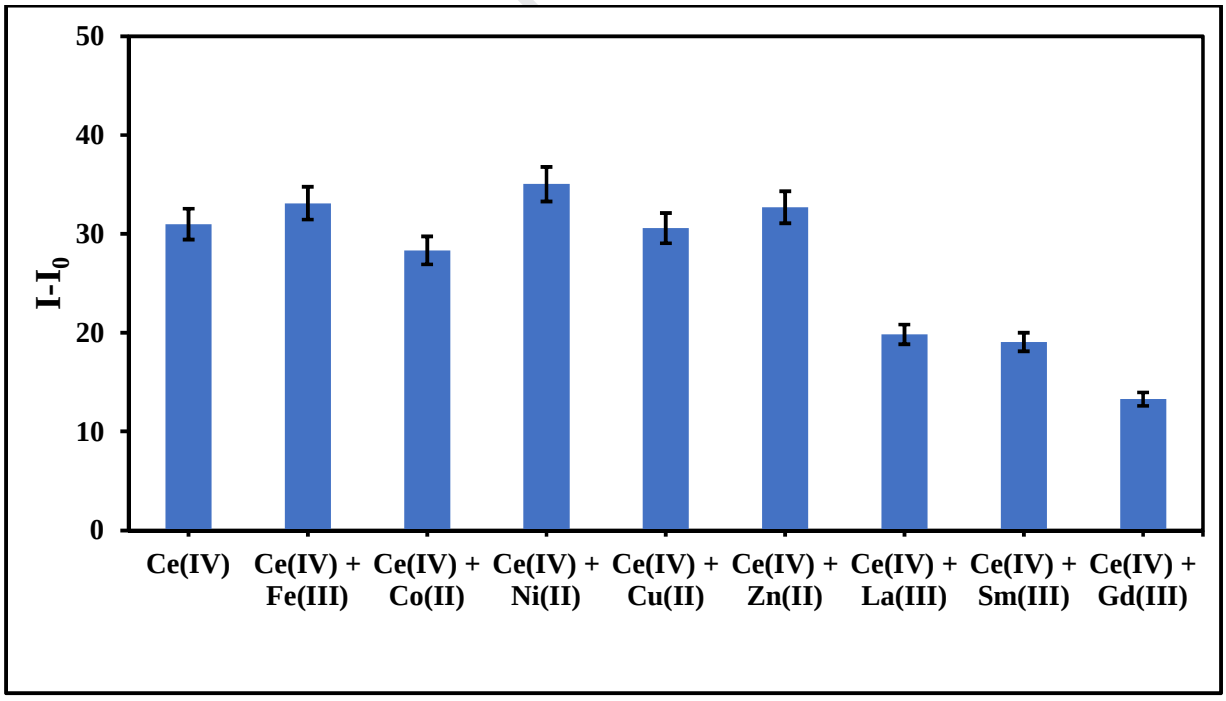

Fig. 15. Effect of interference from equimolar concentration of other metal ions towards fluorimetric sensing of Ce(IV) at pH 7 (0.95 µM each).

Table 1

Comparison of previously reported sensing methods of cerium and dysprosium.

Lantha noid (s)	Reagent(s)/ Condition	Technique	LOD	Major interfering ion(s)	Ref
Ce(IV)	$AgNO_3$, $K_2S_2O_8$ and SiC chip, 1 N H_2SO_4	Spectrophotometry	10^{-5} M	Fe(II)	[22]
Ce(III)	N,N′-bis[2-(salicylidene amino)ethyl]ethane-1,2-diamine, OA[a] and *o*-NPOE[b], pH range 3 to 8	Ce(III)-ion selective membrane electrode	8.91×10^{-8} M	La(III)	[23]
Ce(III)	EDTA[c] and DTTA[d], pH 4	Conductometry	10^{-5} M	Al(III)	[24]
Ce(III)	Quinine sulfate and HIBA[e], pH 2.8 to 3.3	Indirect laser-induced fluorescence	6×10^{-9} M	---	[25]
Ce	*peri*-dihydroxynaphthindenone reagent, pH 2 to 7	Spectrophotometry, potentiometry and gravimetry	10^{-6} M	No significant interference	[26]
Dy(III)	N,N-bis(pyrrolidene) benzne-1,2-diamine, PVC[f] and BA[g], pH range 3.5 to 8	Dy(III)-ion selective membrane electrode	6×10^{-6} M	No significant interference	[27]
Dy(III)	BBH[h] and triacetylcellulose, pH 3 to 5	Optical membrane sensor	3.5×10^{-7} M	No significant interference	[28]
Dy(III)	DPA[i] and SDS[j], pH 11	Luminescence spectroscopy	10^{-12} M	---	[29]
Dy	$Ca(NO_3)_2$ and NH_4F, 1 day aging in acidic pH	Laser excitation of precipitates	10^{-9} M	Ag, Al, Ba, Ca, Cd, Ce, Co, Cr, Cs, Cu, Fe, K, Li, Mg, Mn, NH_4^+, Na, Ni, Pb, Sc, Sr, Th, Y, La, Zn	[30]
Ce(III) and Dy(III)	Laser pulse (10^{-8} to 10^{-9} s), 4.5 M H_2SO_4	Time-resolved laser-induced luminescence and chemiluminescence spectroscopy	10^{-9} M for Ce(III) and 10^{-10} M for Dy(III)	---	[31]
Ce and Dy	poly(norbornene-block-7-oxanorborn-2-ene-5,6-dicarboxylic acid)-coated silica-based sorbents and beaded polymers based on poly(norborn-2-ene-5,6-	High Performance Liquid Chromatography	10^{-6} M	Cu(II), Zn(II), Ni(II), Mn(II)	[32]

	dicarboxylic acid-co-1,4,4a,5,8,8a-hexahydro-1,4,5,8-exo-endo-dimethanonaphthalene), pH 3.5 to 5.5				
Ce and Dy	HIBA[k] and cupferron, pH 3.5 to 5.3	Capillary zone electrophoresis	10^{-6} M	---	[33]
Ce and Dy	CB[l] and THAM [m] buffer, pH 8	Fluorescence spectrscopy	10^{-6} M	Mn(II), Fe(II), Co(II), Ni(II), Cu(II) and Zn(II)	[34]
Ce(IV), Ce(III) and Dy(III)	$RuCl_3.xH_2O$ and morin hydrate, pH range 2, 7 and 12	Absorption and emission spectral method	10^{-6} M	No significant interference	This work

a= oleic acid, b = *o*-nitrophenyloctyl ether, c = ethylenediaminetetraacetic acid, d = trans-1,2-diaminocyclohexanetetraacetic acid, e = α-hydroxyisobutyric acid, f = poly(vinyl chloride), g = benzylacetate, h = N′-[(2-hydroxyphenyl)methylene] benzohydrazide, i = 2,6-pyridinedicarboxylicacid, j = sodium dodecylsulfate, k = hydroxyisobutyric acid, l = calceinblue dye, m = tris(hydroxymethyl)aminomethane

Table 2

Concentration of polyphenol and ruthenium(III) after nanocomposite formation and examined stoichiometry for both Set A and Set B.

Sample	**Concentration of reacted ruthenium(III) (mM)**	**Concentration of reacted polyphenol (mM)**	**Stoichiometry (metal:polyphenol)**
Set A	1.35	1.19	1:0.88
Set B	3.76	3.67	1:0.98

Table 3

Band gap value for ruthenium-morin interaction at different pH.

pH	pH 5	pH 7	pH 9	pH 12
Band Gap (eV)	5.55	5.59	5.64	5.68

Table 4

FTIR spectral data of the pure morin and prepared ruthenium-morin nanocomposites with their possible functionalities.

Sample	Peak Position (cm^{-1})	Functionality
Set B	3451	Sharp, due to O-H stretching frequency [2]
	2061 1994 1943	Ru-CO bond frequency [48]
	1627	C=O stretching frequency [48, 49]
	1510 1452	In plane O-H bending + aromatic C=C stretching [50, 51]
	1177	Aromatic C-H bending [52]
Set A	3453	Sharp, due to O-H stretching frequency [2]
	2067 1990 1867	Ru-CO bond frequency [48]
	1619	C=O stretching frequency [48, 49]
	1383	-OH bending vibration and in plane bending vibration of C-O-H group [48]
	1121	-C-O-C stretching [52]
Pure Morin	3405	Broad, due to H-bonded O-H group stretching frequency [2]
	1612	C=O stretching frequency [48, 49]
	1515 1445	Aromatic C=C stretching and in plane C-C-H bending [50, 51]
	1376	-OH bending vibration and in plane bending vibration of C-O-H group [48]
	1294	Asymmetric stretching of Ph-O bond [52]
	1163	Aromatic C-H bending [52]
	831	Twisting of C-O bond [53]

Table 5

Atomic percentage of $RuCl_3$ and RuO_3 present in Set A and Set B obtained from XPS analysis.

Sample	Atomic %	
	$RuCl_3$	**RuO_3**
Set A	72.6 ± 4.6	27.4 ± 4.6
Set B	58.6 ± 2.3	41.4 ± 2.3

Table 6

Atomic percentage of different type of carbon atom present in Set A and Set B obtained from XPS analysis.

Sample	Atomic %				
	sp^2 Carbon	**sp^3 Carbon**	**C-O-C, C-OH**	**C=O**	**O-C=O**
Set A	43.9 ± 2.2	11.5 ± 1.5	24.3 ± 0.2	14.0 ± 0.5	6.4 ± 0.0
Set B	33.6 ± 2.7	16.1 ± 3.2	23.1 ± 1.5	17.5 ± 0.9	9.7 ± 0.1

Table 7

Different analytical parameters for the detection of the Ce(IV) using Set B nanocomposite at different pH.

Parameter	UV-metric			Fluorimetric
	pH 2	**pH 7**	**pH 12**	**pH 7**
Regression equation	Y = sX	Y = sX	Y = sX	Y = sX
Slope (s) ($mmol^{-1}$)	2.36	8.49	92.18	26,965.00
Correlation coefficient (R^2)	0.98	0.99	0.96	0.95
Standard deviation (σ)	0.008	0.002	0.003	2.867
Limit of detection (LOD = 3.3× σ/s (μmol)	13.24	1.03	0.09	0.35
Limit of quantification (LOQ = 10× σ/s (μmol)	40.13	3.15	0.29	1.06

Linear range (μmol)	34.40 to 92.67	2.37 to 11.74	0.12 to 0.37	0.49 to 2.35
λ (nm)	λ_{max} (nm) 293	λ_{max} (nm) 293	λ_{max} (nm) 320	λ_{ex} (nm) 290 λ_{em} (nm) 391

Table 8

Different analytical parameters for the detection of the Ce(III) and Dy(III) under UV-metric method using Set B nanocomposite at different pH.

Parameter	**Dy(III)**	**Ce(III)**
	pH 2	**pH 12**
Regression equation	Y = sX	Y = sX
Slope (s) ($mmol^{-1}$)	4.96	26.97
Correlation coefficient (R^2)	0.98	0.98
Standard deviation (σ)	0.008	0.001
Limit of detection (LOD = 3.3× σ/s (μmol)	5.37	0.08
Limit of quantification (LOQ = 10× σ/s (μmol)	16.28	0.25
Linear range (μmol)	11.74 to 34.40	0.12 to 0.61
λ_{max} (nm)	293	293

Table 9

Change of band gap on sensing of Ce(III), Ce(IV) and Dy(III) at different pH.

Band gap of the nanoparticle (eV)	**Change of Band gap on sensing (eV)**				
	Sensing at pH 2		**Sensing at pH 7**	**Sensing at pH 12**	
	Ce(IV)	**Dy(III)**	**Ce(IV)**	**Ce(IV)**	**Ce(III)**
5.68	5.13	5.38	5.63	5.64	5.22

Table 10

Analysis of environmental samples.

Sample	pH	Measured lanthanoids	Added (μM)	Found (μM)	Recovery (%)
Tap water	2	Ce(IV)	---	---	---
			49.00	48.90	99.80
			110.00	108.88	98.98
			129.00	127.22	98.62
		Dy(III)	---	---	---
			47.20	45.19	95.74
			56.10	53.79	95.88
			64.80	63.76	98.40
	7	Ce(IV)	---	---	---
			14.60	13.85	94.87
			19.40	19.12	98.56
			24.20	25.17	104.00
	12	Ce(IV)	---	---	---
			0.25	0.21	80.61
			0.74	0.78	105.95
			0.86	0.84	97.24
		Ce(III)	---	---	---
			0.49	0.42	86.21
			0.74	0.65	87.65
			1.09	1.13	103.92
Ground Water	2	Ce(IV)	---	---	---
			110.00	111.03	100.94
			129.00	124.89	96.81
			148.00	143.67	97.07
		Dy(III)	---	---	---
			19.40	18.91	97.50
			38.10	38.38	100.73
			47.20	46.91	99.39
	7	Ce(IV)	---	---	---
			17.00	16.92	99.52
			19.40	18.47	95.23
			21.80	21.98	100.82
	12	Ce(IV)	---	---	---
			0.30	0.33	109.11
			0.37	0.39	105.41
			0.49	0.45	91.38

Highlights

- Ru-morin nanocomposites were synthesized in presence and absence of γ-radiation.
- Smaller particles with smaller pores were formed in presence of γ-radiation.
- The irradiated nanocomposite was suitable for analytical sensing.
- Sensing of Ce(IV), Ce(III), Dy(III) out of different lanthanoids is pH dependent.

Declaration of interests

☑The authors declare that they have no known competing financial interests or personal relationships that could have appeared to influence the work reported in this paper.

☐The authors declare the following financial interests/personal relationships which may be considered as potential competing interests: